

# Searching for New Cataclysmic Variables in the Chandra Source Catalog

Ilkham Galiullin<sup>1</sup>, Antonio C. Rodriguez<sup>2</sup>, Kareem El-Badry<sup>2</sup>, Paula Szkody<sup>3</sup>, Abhijeet Anand<sup>4</sup>, Jan van Roestel<sup>5</sup>, Askar Sibgatullin<sup>1</sup>, Vladislav Dodon<sup>1</sup>, Nikita Tyrin<sup>1</sup>, Iaria Caiazzo<sup>2</sup>, Matthew J. Graham<sup>2</sup>, Russ R. Laher<sup>6</sup>, Shrinivas R. Kulkarni<sup>2</sup>, Thomas A. Prince<sup>7</sup>, Reed Riddle<sup>2</sup>, Zachary P. Vanderbosch<sup>2</sup> and Avery Wold<sup>2</sup>

<sup>1</sup> Kazan Federal University, Kremlevskaya Str.18, 420008, Kazan, Russia  
e-mail: IlhIGaliullin@kpfu.ru

<sup>2</sup> Department of Astronomy, California Institute of Technology, 1200 E. California Blvd, Pasadena, CA, 91125, USA

<sup>3</sup> Department of Astronomy, University of Washington, 3910 15th Avenue NE, Seattle, WA 98195, USA

<sup>4</sup> Lawrence Berkeley National Laboratory, 1 Cyclotron Road, Berkeley, CA 94720, USA

<sup>5</sup> Anton Pannekoek Institute for Astronomy, University of Amsterdam, 1090 GE Amsterdam, The Netherlands

<sup>6</sup> IPAC, California Institute of Technology, 1200 E. California Blvd, Pasadena, CA 91125, USA

<sup>7</sup> Division of Physics, Mathematics, and Astronomy, California Institute of Technology, Pasadena, CA 91125, USA

Received XXX; accepted XXX

## ABSTRACT

**Aims.** Cataclysmic variables (CVs) are compact binary systems in which a white dwarf accretes matter from a Roche-lobe-filling companion star. In this study, we searched for new CVs in the Milky Way in the *Chandra* Source Catalog v2.0, cross-matched with *Gaia* Data Release 3 (DR3).

**Methods.** We identified new CV candidates by combining X-ray and optical data in a color-color diagram called the “X-ray Main Sequence”. We used two different cuts in this diagram to compile pure and optically variable samples of CV candidates. We undertook optical spectroscopic follow-up observations with the Keck and Palomar Observatories to confirm the nature of these sources.

**Results.** We assembled a sample of 25,887 Galactic X-ray sources and found 14 new CV candidates. Seven objects show X-ray and/or optical variability. All sources show X-ray luminosity in the  $10^{29} - 10^{32}$  erg s<sup>-1</sup> range, and their X-ray spectra can be approximated by a power-law model with photon indices in the  $\Gamma \sim 1 - 3$  range or an optically thin thermal emission model in the  $kT \sim 1 - 70$  keV range. We spectroscopically confirmed four CVs, discovering two new polars, one low accretion rate polar and a WZ Sge-like low accretion rate CV. X-ray and optical properties of the other 9 objects suggest that they are also CVs (likely magnetic or dwarf novae), and one other object could be an eclipsing binary, but revealing their true nature requires further observations.

**Conclusions.** These results show that a joint X-ray and optical analysis can be a powerful tool for finding new CVs in large X-ray and optical catalogs. X-ray observations such as those by *Chandra* are particularly efficient at discovering magnetic and low accretion rate CVs, which could be missed by purely optical surveys.

**Key words.** novae, cataclysmic variables – Stars: dwarf novae – X-rays: binaries – binaries: close – white dwarfs – binaries: eclipsing

## 1. Introduction

Cataclysmic variables (CVs) are compact semi-detached binaries in which a white dwarf (WD) accretes matter from a Roche-lobe filling companion star (Warner 2003). CVs have orbital periods, typically spanning 66 min – 10 hr, except for ultra-compact AM Canum Venaticorum (AM CVn) stars, which possess  $\lesssim 1$  hr periods (Ramsay et al. 2018). In magnetic CVs, the magnetic field of the WD ( $B \gtrsim 1$  MG) significantly influences the accretion onto the surface of the WD. Magnetic CVs are split into intermediate polars (IP) with truncated disks, and polars, where the strong field ( $B \sim 10 - 250$  MG) prevents disk formation. Studies of CVs augment our understanding of various astrophysical phenomena, including their role as potential progenitors for Type Ia supernovae (Maoz et al. 2014). They also present optimal non-relativistic laboratories to study accretion processes (Hameury 2020). Furthermore, due to their short orbital periods, some CVs and many ultra-compact AM CVn systems are classified as prospective “verification binaries” for fu-

ture planned space-based gravitational wave observatories such as LISA (Kupfer et al. 2023).

From the theoretical standpoint, CVs are predicted to form as a result of Common Envelope Evolution (CEE) (Paczynski 1976; Ivanova et al. 2013) that first brings the stars closer together. Angular momentum loss (AML) is the key factor in the long-timescale evolution of CVs. As AML occurs, the separation between the stars decreases, leading to a reduction in the orbital period. The evolutionary model considers two mechanisms for AML: Magnetic wind Braking (MB) (Rappaport et al. 1983; Spruit & Ritter 1983) and Gravitational-wave Radiation (GR) (Paczynski 1967; Faulkner 1971). Although the model initially aligned well with the observational data of that era, subsequent findings revealed numerous discrepancies between theory and observations (e.g., Patterson 1998; Gänsicke et al. 2009; Pretorius & Knigge 2012; El-Badry et al. 2022). Consequently, empirical revisions were proposed to rectify these inconsistencies (e.g., Knigge et al. 2011; Schreiber et al. 2016, 2021).

CVs exhibit a broad range of observational features, therefore detailed multiwavelength studies are necessary to draw

accurate conclusions about their nature and population. X-ray emission analysis is a powerful tool for searching for and studying CVs. The first X-ray observations of CVs took place with HEAO-1 (Cordova et al. 1981) and Einstein (Cordova & Mason 1984). Early X-ray surveys led to the discovery of a unique, previously unidentified population of magnetic CVs (e.g., Haberl & Motch 1995). The all-sky X-ray survey conducted by the eROSITA telescope aboard the Spektrum-Roentgen-Gamma (SRG) mission (Sunyaev et al. 2021; Predehl et al. 2021) is proving to be groundbreaking by cataloging millions of sources (Merloni et al. 2024) and has already been successful in discovering a collection of new and rare CVs due to its ability to reach much fainter fluxes (e.g., Schwöpe et al. 2022a,b; Rodriguez et al. 2023a; Galiullin et al. 2024).

Despite not being an all-sky X-ray survey, the *Chandra* observatory provides unique sub-arcsecond on-axis resolution which is comparable with optical surveys (Weisskopf et al. 2000, 2002). The *Chandra Source Catalog v2.0* (hereafter, CSC2) provides the uniformly calibrated, science-ready data products compiled from the archival *Chandra* data (Evans et al. 2010). Such data collection enables the study of properties of X-ray sources with spectral and timing analyses and classifying new objects in the catalog. In addition to new X-ray surveys and catalogs, all-sky optical photometric surveys provide a wealth of new data. The Zwicky Transient Facility (ZTF) is the deepest Northern sky time-domain photometric survey, conducted at Palomar Observatory on the Samuel Oschin 48-inch telescope. The 47 deg<sup>2</sup> field-of-view camera images the sky roughly every two days down to ~20.5 mag in *g*, *r*, and *i* filters (Bellm et al. 2019; Graham et al. 2019; Dekany et al. 2020; Masci et al. 2019).

In this paper, we aim to search for and study new CVs in the CSC2, cross-matched with the third *Gaia* Data Release (hereafter, *Gaia* DR3). In Section 2, we describe the construction steps of a sample of Galactic X-ray sources based on the CSC2–*Gaia* DR3 catalog. In Section 3, we describe the selection of new CV candidates in the CSC2–*Gaia* DR3 catalog using two different cuts in the X-ray and optical color-color diagram, known as the “X-ray Main Sequence”. We compile pure and optically variable samples of CV candidates. In Section 4, we present the follow-up observations conducted with the 5m Hale Telescope at Palomar Observatory and the 10m Keck I Telescope on Mauna Kea. We also present detailed X-ray timing and spectroscopic analyses. In Section 5, we present the sample of 14 CV candidates found in the CSC2–*Gaia* DR3 catalog. We separately discuss the nature of four spectroscopically confirmed CVs and four variable CV candidates. Our results are summarized in Section 6.

## 2. Sample of Galactic X-ray sources

We began by constructing a sample of Galactic X-ray sources from the publicly available CSC2 (Evans et al. 2010). We cross-matched CSC2 with the *Gaia* DR3 catalog (Gaia Collaboration et al. 2023), keeping only objects with significant parallaxes and proper motions. We identified the known sources in our sample by cross-matching with the Simbad database and other publicly available CV catalogs. All sample creation steps are presented in detail below.

### 2.1. *Chandra* Source Catalog

As a first step, we used the master source table from the CSC2 with a total of about ~ 317,000 unique source detections. We set

the following criteria<sup>1</sup> to select the point-like X-ray sources with measured parameters:

1. `extent_flag` = False; only point-like sources.
2. `conf_flag` = False; source regions do NOT overlap.
3. `pileup_flag` = False; ACIS pile-up fraction does NOT exceed ~ 10% in all observations.
4. `sat_src_flag` = False; the source is NOT saturated in all observations.
5. `streak_src_flag` = False; the source is NOT located on an ACIS readout streak in all observations.
6. `dither_warning_flag` = False; highest statistically significant peak in the power spectrum of the source region count rate does NOT occur at the dither frequency of the observation.
7. `man_add_flag` = False and `man_inc_flag` = False; the source was NOT manually added nor included in the catalog via human review.
8. `man_match_flag` = False; source detections were NOT manually matched between overlapping stacked observations via human review.
9. `man_pos_flag` = False; best-fit source position was NOT manually modified via human review.
10. `man_reg_flag` = False; source region parameters were NOT manually modified via human review.

Using these criteria, we selected 271,438 unique objects from CSC2.

### 2.2. Cross-match with *Gaia*

For the next step, we cross-matched 271,438 objects with the *Gaia* DR3 catalog (Gaia Collaboration et al. 2023) to select only Galactic sources. As a search radius for each object, we used the individual X-ray positional error (with a search radius equal to `err_ellipse_r0`, the semi-major axis of the 95% confidence ellipse). We only kept sources meeting the following criteria:

1.  $\text{RUWE} < 1.4$  (as recommended in Gaia Collaboration et al. 2023); good fit to the astrometric observations.
2. Only ONE *Gaia* object must be within the search radius.
3. Parallax and proper motion are measured with a signal-to-noise ratio  $S/N \geq 3$ .

These selection steps reduced the number of sources to 26,079. To remove any potential high proper motion stars, we applied an additional filtering criterion:

1.  $\text{pm} \times \Delta t \leq \text{err\_ellipse\_r0}$ ; The angular motion of the *Gaia* object (caused by a proper motion (pm)) during the time interval  $\Delta t$  does not exceed the search radius (`err_ellipse_r0`). The time interval  $\Delta t$  is an epoch difference between *Gaia* DR3 (Epoch 2016) and CSC2 (Epoch 2000) catalogs.

This filter finally resulted in 25,887 objects in the CSC2–*Gaia* DR3 catalog.

<sup>1</sup> For detailed flag descriptions see Evans et al. (2010) and CSC2 web-page: <https://cxc.cfa.harvard.edu/csc/columns/flags.html>

### 2.3. Identification of Known Sources

To identify known sources in the CSC2–*Gaia* DR3 catalog, we cross-matched our objects with the Simbad database (Wenger et al. 2000) using *Gaia* coordinates and a 3'' search radius. We grouped our objects based on the Simbad hierarchical structure<sup>2</sup>, making seven general types: STARS (single and binaries), ACCRETING BINARIES (X-ray binaries, CVs, Nova and Symbiotic Stars), GALAXY, ISM, PROPERTIES, BLENDS (not well-defined objects) and UNKNOWN (object is not presented in Simbad database). In Appendix A, we present a detailed description of our general object types compiled from the Simbad hierarchical structure. We found Simbad classifications for 12,181<sup>3</sup> of the 25,887 objects. 32 of these 12,181 were known CVs or CV candidates.

To check that we did not miss any known CVs, we independently cross-matched our 25,887 objects with the following catalogs using a 2'' search radius: i) *Ritter and Kolb catalog* (Ritter & Kolb 2003) (Final version; December 31, 2015); ii) *Cataclysmic Variables Catalog* (2006 edition; Downes et al. (2001)); iii) *The Open Cataclysmic Variable catalog* (Jackim et al. 2020) (only confirmed CVs are kept in the list). We combined the information from the Simbad database and these three CV catalogs to make the final list of known CVs. Out of 25,887 sources, we finally compiled a sample of 40 known CVs. This sample of 40 consists of the CVs from Simbad plus those from the three catalogs mentioned above.

We note that 52 objects (out of 25,887) were classified as GALAXY. These objects are primarily quasars and galaxies hosting active galactic nuclei that show significant parallax and proper motion. The high proper motions and parallaxes of these extragalactic objects could be due to variability-induced motion (e.g., Souchay et al. 2022; Makarov & Secrest 2022; Khamitov et al. 2023). Detailed investigation of these objects is beyond the scope of this paper.

### 3. CV Selection with the X-ray Main Sequence

We combined X-ray and optical data to search for new CV candidates in the CSC2–*Gaia* DR3 catalog. We used the “X-ray Main Sequence”, a phase space of X-ray-to-optical flux ratio ( $F_X/F_{\text{opt}}$ ) and a *Gaia* optical BP–RP color (Rodriguez 2024), to select CV candidates and create a pure sample of these objects. The empirical cut in the “X-ray Main Sequence” is given by the following functional form,

$$\log(F_X/F_{\text{opt}})_{\text{cut}} = A + B \times (BP - RP), \quad (1)$$

where  $A = -3.5$  and  $B = 1$  are linear parameters from Rodriguez (2024). We computed the  $F_X/F_{\text{opt}}$  ratio based on X-ray and *Gaia* optical fluxes. The X-ray fluxes were calculated in the 0.5–7 keV energy band from CSC2. The aperture-corrected (90% enclosed counts fraction) energy flux is calculated using the power-law model with a photon-index of  $\Gamma = 2$  and the individual Galactic hydrogen column density  $N_{\text{H(Gal)}}$  in the direction of the source. *Gaia* G band magnitudes were converted to optical fluxes using

the AB magnitude system and a central wavelength of 6,000 Å. Out of 25,887 sources in the CSC2–*Gaia* DR3 catalog, we selected only sources with measured X-ray fluxes and optical magnitudes:

1.  $\text{flux\_powlaw\_aper90\_b/error} \geq 2$ ; Source X-ray flux in the 0.5–7 keV energy band is measured with signal-to-noise ratio more than  $S/N \geq 2$ .
2. *Gaia* G band, BP and RP magnitudes are measured having signal-to-noise ratio more than  $S/N \geq 2$ .

These selection steps finally resulted in 19,665 sources (with 36 known CVs).

#### 3.1. First Selection: A pure sample of CV candidates

To compile a pure sample of CV candidates and avoid contamination from stellar objects, we searched for optimal values for linear parameters A and B in Eq. 1. We created two samples of known sources classified based on the Simbad hierarchical structure: one consisting of CVs (36 sources) and the other of stellar objects (STARS, 4781 sources). For the STARS sample, we included only objects with sub-types classified as "YSO", "Binaries", "Massive Stars", "Main-sequence Stars", or "Evolved Stars" (see Table A.1). The left panel of Figure 1 shows an  $F_X/F_{\text{opt}}$  and *Gaia* BP–RP color diagram for known CVs (red squares) and STARS (blue dots). It's evident that known CVs are primarily located in the upper left corner of the diagram and could be visually separated from STARS. We computed the purity and completeness using a sample of these known CVs and STARS (see Appendix A for more details). Based on our completeness/purity analysis we selected  $A = -1.5$ , and  $B = 0.7$  that gives the highest purity ( $\approx 100\%$ ) and  $\approx 52\%$  completeness.

We only searched for new CV candidates among objects without precise classification from the Simbad database. Out of 19,665 objects, we selected 13,956 sources classified as one of the following object types: i) UNKNOWN (9,868 sources); ii) PROPERTIES (355 sources); iii) STARS, sub-type "Star" (3,720 sources); iv) STARS, sub-type "WD" (10 sources); v) STARS, sub-type "BD" (3 sources). The right panel of Figure 1 shows the  $F_X/F_{\text{opt}}$  and *Gaia* BP–RP color diagram for these objects. We found 11 new CV candidates (out of 13,956 objects) with our selection based on our most optimal values for  $A = -1.5$  and  $B = 0.7$  (see objects above the solid red line in the right panel of Figure 1).

We note that we independently found three objects (recently confirmed as CVs) as CV candidates using the  $F_X/F_{\text{opt}}$  and *Gaia* (BP–RP) color diagram. During the writing of this manuscript, we learned that these systems had been previously discovered. However, these objects have only been mentioned in one or two papers, so we included those objects in our analysis and discussed them individually in Appendix B.

#### 3.2. Second Selection: An optically variable sample of CV candidates with ZTF photometry

Many CVs appear as periodic sources in optical light curves. Furthermore, accretion can lead to outbursts, which can also be observed in their optical light curves, particularly in non-magnetic CVs. Therefore, even after compiling a sample of 11 CV candidates based purely on an  $F_X/F_{\text{opt}}$  and *Gaia* BP–RP color diagram, we also searched for possible variability in a larger sample of sources. We used the empirical cut on the  $F_X/F_{\text{opt}}$  and *Gaia* BP–RP color diagram from Rodriguez (2024)

<sup>2</sup> <http://simbad.cds.unistra.fr/guide/otypes.htm>

<sup>3</sup> While creating the catalog of known systems, we had multiple matches (more than one) within the search radius for 810 of the 12,181 objects, giving about 7% of possible spurious associations in the catalog. However, for most objects with multiple matches a Simbad database provided a similar main object type (as defined in Table A.1). We adopted the Simbad object type from the nearest source for those objects.

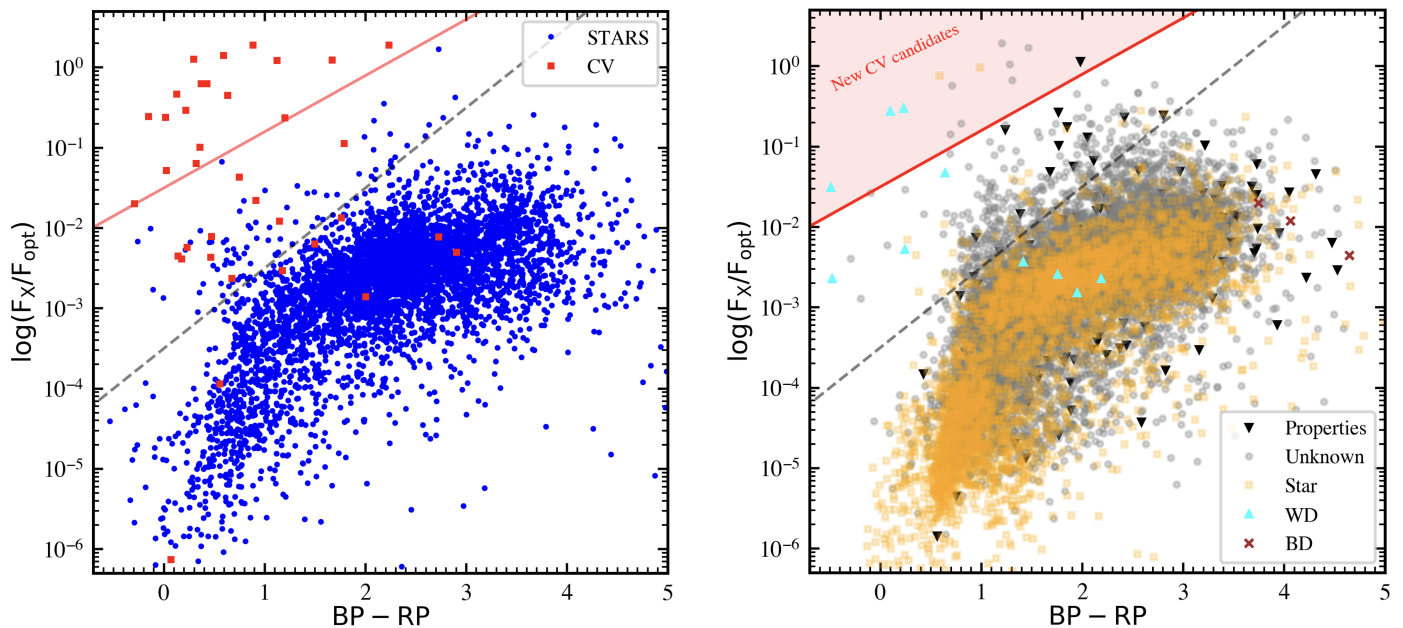


**Fig. 1.** X-ray-to-optical flux ratio vs *Gaia* (BP–RP) optical color (X-ray Main Sequence; Rodriguez 2024) for objects in the CSC2–*Gaia* DR3 catalog. *Left panel:* Known CVs (red) and stellar objects (STARS, blue) in the CSC2–*Gaia* DR3 catalog. *The dashed black line* shows an empirical cut from Rodriguez (2024). *The solid red line* shows a cut to select a pure sample of CV candidates. *Right panel:* Objects in the CSC2–*Gaia* DR3 catalog with the Simbad classifications (which may be imprecise). *Color symbols* correspond to the different object types based on the Simbad hierarchical structure (see Table A.1 in Appendix A). Objects above *the solid red line* and variable objects above *the dashed black line* are classified as new CV candidates (see Table 1 and Table B.1). For more details, see Section 3.

( $A = -3.5$  and  $B = 1$ ) and searched for possible variability in 375 sources (see objects above the dashed black line in the right panel of Figure 1).

We searched for periodic and outbursting-type variability in sources based on ZTF optical photometry for both  $g$  and  $r$  light curves, considering only data with a signal-to-noise ratio greater than 5,  $\text{SNR}_{\text{ZTF}} > 5$ . We retrieved ZTF light curves for our objects and used the barycentric corrected modified Julian date (MJD) in our analysis. Light curves have a photometric precision of  $\sim 0.015$  mag at the bright limit of 14 mag, decreasing to a precision of  $\sim 0.1$  mag at the faint limit of 20.5 mag. We searched for periodic variability using the Lomb-Scargle periodogram, as implemented in the *gatspy* tool to search for periods ranging from 5 min to 10 days. Once the period search was performed, we excluded all sources with orbital periods that are multiples or fractions of the sidereal day. To first order, the periods are reported up to a precision of 30 sec, which is determined by the exposure time. To calculate the significance of a period, we first computed the median absolute deviation (MAD) of the periodogram. Then, we took the periodogram value at the highest peak and divided it by the MAD. This ratio served as our significance metric. We plotted the distribution of significance metrics and kept only those sources in the upper 80<sup>th</sup> percentile of the distribution. To search for outbursting sources, we looked for ZTF light curves with more than 5 outburst points  $\Delta\text{mag} \geq 1$ , with each point more than 3 standard deviations from the median.

In total, we had 178 (out of 375) sources with ZTF photometry. Using our selection criterion described above, we found five periodic sources (see Figures 2, 5, 7 and 8). With ZTF photometry, only one outbursting source (2CXO J024131.0+593630) was identified, which we discuss in Appendix B. Based on the analy-

sis of optical ZTF light curves, we extended our final sample of CV candidates to include a total of 14 candidates<sup>4</sup>.

Out of 14 sources, 2 objects were marked as variables with a *Gaia* flag (`phot_variable_flag = VARIABLE`). These objects show outbursting-type variability. Figure 3 shows optical light curves based on *Gaia* photometry ( $\text{SNR}_{\text{Gaia}} > 3$ ). Table 1 (column 9) summarizes the variability properties of the sources in the final sample. We note that the number of spurious matches in our final sample is effectively zero due to the  $\sim 1$ – $2''$  localization of X-ray sources made possible by *Chandra*. Furthermore, our candidates that show optical variability are even less likely to be false matches, since optical variable sources, particularly accreting compact objects, are typically associated with X-ray emission (e.g., see Figure 2 of Rodriguez (2024)).

## 4. Data and Analysis

### 4.1. Optical Spectra

We performed optical spectroscopic follow-up observations for four sources in our sample, focusing on those located in the Northern Hemisphere that were accessible to our telescopes and exhibited strong optical variability and/or a high  $F_x/F_{\text{opt}}$  ratio. We used both the Double Spectrograph (DBSP; Oke & Gunn 1982) on the 5m Hale Telescope at Palomar Observatory and the Low-Resolution Imaging Spectrometer (LRIS; Oke et al. 1995) at the 10m Keck I Telescope on Mauna Kea. During all DBSP observations, we used the 600/4000 grism on the blue side and the 316/7500 grating on the red side. A  $1.5''$  slit was used, and the seeing on all occasions was  $1.5$ – $2.0''$ . All P200/DBSP data

<sup>4</sup> Two periodic sources were already presented in the sample of 11 new CV candidates (selected by  $F_x/F_{\text{opt}}$  and *Gaia* BP–RP color). Therefore, we added only three variable sources (out of five) in our final sample to include 14 CV candidates in total.

**Table 1.** List of new CVs and their candidates found in the CSC2–*Gaia* DR3 catalog.

Object ID (2CXO)	R.A.	DEC.	R <sub>95</sub> (")	<i>Gaia</i> DR3 source_id	G (mag)	BP–RP (mag)	F <sub>X</sub> /F <sub>opt</sub> (8)	Var. (9)	d (pc)	L <sub>X</sub> (10 <sup>30</sup> erg s <sup>-1</sup> )	Obj. Type	Opt. Spec.
(1)	(2)	(3)	(4)	(5)	(6)	(7)	(8)	(9)	(10)	(11)	(12)	(13)
<i>CV candidates selected via F<sub>X</sub>/F<sub>opt</sub> ratio and Gaia (BP–RP) color (First cut)</i>												
J044147.9–015145	04 41 47.9	–01 51 45.7	0.92	3229135015053480064	20.27	0.10	0.27	–	249 ± 42	0.31 ± 0.12	4	✓
J063805.1–801854	06 38 05.2	–80 18 54.1	0.75	5207809444546340096	20.09	0.59	0.76	Xt/Ga	858 ± 181	23.73 ± 10.10	3	
J094607.7–311550	09 46 07.8	–31 15 50.9	4.61	5440027429908157440	19.62	–0.49	0.03	–	498 ± 91	0.39 ± 0.18	3	
J104435.5–594045	10 44 35.6	–59 40 45.7	1.03	5350359031173784704	19.03	–1.91*	0.01	–	755 ± 161	0.22 ± 0.11	3	
J123727.5+655211	12 37 27.5	+65 52 11.9	0.87	1680514565693517696	19.18	1.28	1.05	2.12 <sup>h</sup> /X	593 ± 57	43.64 ± 8.48	1	✓
J155926.5–754311	15 59 26.6	–75 43 11.5	6.97	5781613222711313152	20.52	0.80	0.20	–	409 ± 108	0.49 ± 0.31	1	
J165219.0–441401	16 52 19.0	–44 14 01.8	0.72	5964348898459271040	18.79	1.98	1.16	Ga	1839 ± 572	303.87 ± 195.30	2	
J173332.5–181735	17 33 32.6	–18 17 35.8	0.71	4123404591191472384	18.61	1.20	1.93	–	855 ± 153	171.65 ± 62.06	1	
J173555.3–292530	17 35 55.3	–29 25 30.2	2.65	4060073129401992832	20.47	0.71	0.57	–	127 ± 26	0.13 ± 0.07	1	
J182117.2–131405	18 21 17.2	–13 14 05.8	1.49	4152650221755630464	20.22	0.69	0.15	2.01 <sup>h</sup>	189 ± 30	0.06 ± 0.03	1	✓
J190823.2+343328	19 08 23.2	+34 33 28.1	2.90	2044505592269020416	20.47	1.30	0.67	–	373 ± 103	1.84 ± 1.05	1	
<i>CV candidates selected via period search (Second cut)</i>												
J044048.3+292434	04 40 48.3	+29 24 34.4	0.72	158134751604204416	18.89	2.22	0.62	1.30 <sup>h**</sup>	296 ± 21	7.05 ± 1.41	1	✓
J173118.6+224248	17 31 18.7	+22 42 48.8	1.63	4557025073462888960	19.70	2.51	0.29	1.84 <sup>h**</sup>	488 ± 75	2.40 ± 0.84	1	
J185603.2+021259	18 56 03.3	+02 12 59.8	2.18	4267156871660419712	17.06	1.33	0.05	5.46 <sup>h</sup>	211 ± 4	0.25 ± 0.09	1	

**Notes.** *Data from CSC2:* (1) Source name, (2) and (3) Source position: right ascension and declination, (4) Major radius of the 95% confidence level position error ellipse; *Data from Gaia DR3:* (5) Source ID, (6) and (7) G band and (BP–RP) magnitudes; (8) X-ray-to-optical flux ratio; (9) Variability flag. Orbital periods (in hr) are computed based on ZTF photometry in this study (see Section 3.2). If object is marked as a variable in: "Ga" – *Gaia* DR3 catalog; "X" – CSC2 catalog; "Xt" – X-ray timing analysis revealed a periodic signal (see Section 4.3); (10) Distance and its 1 $\sigma$  uncertainty computed from the *Gaia* parallax; (11) Absorption-corrected X-ray luminosity in the 0.5–7 keV energy band and its 1 $\sigma$  uncertainty; (12) Main object type based on Simbad database (see Section 2.3 and Table A.1): 1 – UNKNOWN; 2 – PROPERTIES; 3 – STARS, sub-type "Star"; 4 – STARS, sub-type "WD"; (13) Source has an optical spectrum (see Section 4.1). (\*) Indicates likely unreliable value due to large measurement errors; therefore, CV candidate 2CXO J104435.5–594045 ( $M_G = 8.9$ ) is not shown in Figures 1 and 10 for illustrative purposes. (\*\*) With our current data, we cannot distinguish between the two orbital periods of the system. The orbital period can be either the current value or two times it.

**Table 2.** Data acquired for CV candidates.

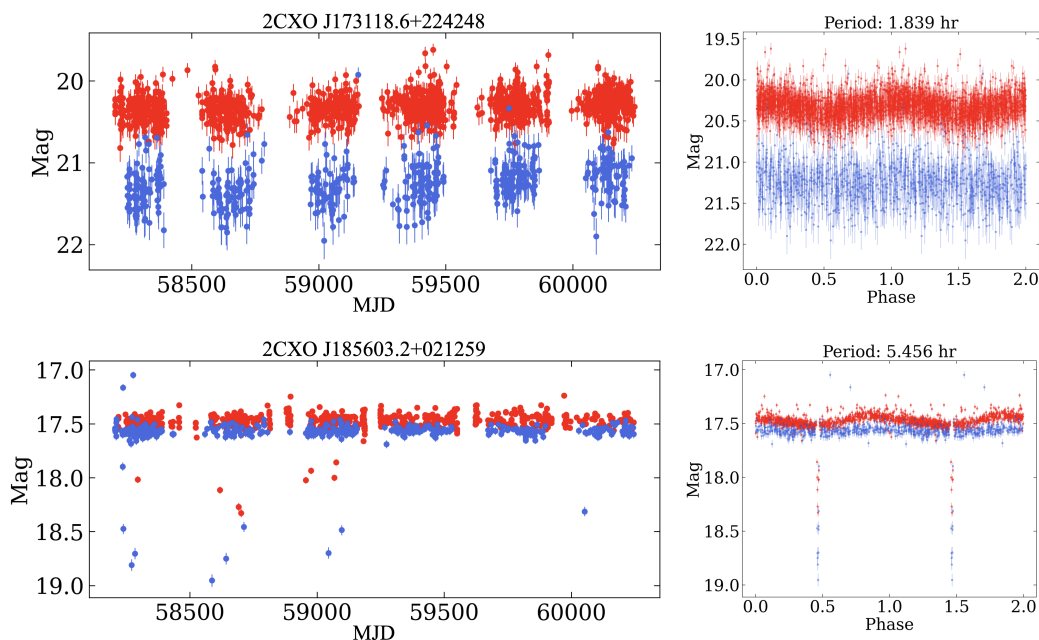
Object ID (2CXO)	Data Type	Date	Instrument	Finding
J044048.3+292434	Identification Spectrum	22 Nov. 2022	P200/DBSP	Hydrogen Balmer and Helium, and high-excitation HeII 4686Å emission lines.
		22 Nov. 2022	P200/DBSP	Two spectra were taken 1.4 hr apart and show no significant radial velocity shift.
J044147.9–015145	Identification Spectrum	16 Nov. 2022	Keck I/LRIS	Hydrogen and Helium emission, along with WD Balmer absorption lines. No detectable HeII 4686Å emission line is seen.
J123727.5+655211	Identification Spectrum	22 Nov. 2022	P200/DBSP	Hydrogen, Helium, and high excitation HeII 4686Å emission lines.
J182117.2–131405	Identification Spectrum	22 May 2023	Keck I/LRIS	The spectrum is dominated by broad humps which correspond to cyclotron harmonics, and no significant $H\beta$ and He II 4686Å emission lines are detected.

were reduced with DBSP-DRP<sup>5</sup>, a Python-based pipeline built upon the existing PyPeIt package (Prochaska et al. 2020) and optimized for reducing spectral data. During all LRIS observations, we used the 600/4000 grism on the blue side and the 600/7500 grating on the red side. We used a 1.0" slit, and the seeing on all occasions was around 0.7". LRIS data were reduced with lpipe, an IDL-based pipeline optimized for LRIS long slit spectroscopy (Perley 2019). All data were flat fielded and sky-subtracted using standard techniques, wavelength-calibrated with internal arc lamps, and flux-calibrated using a standard star.

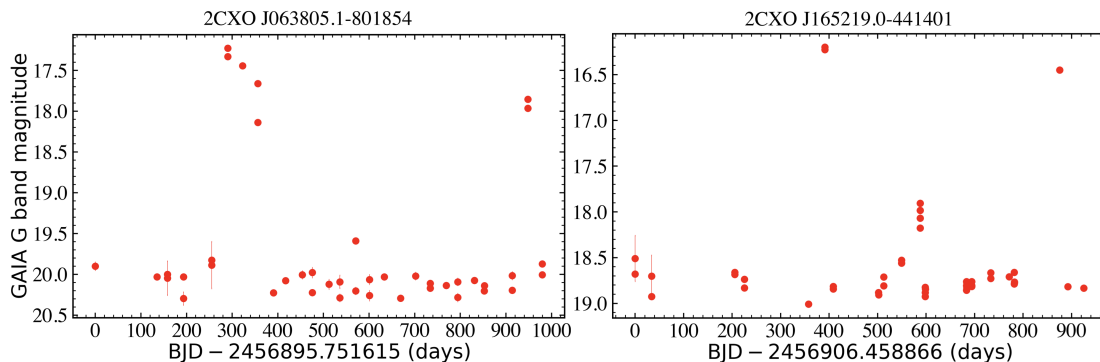
<sup>5</sup> <https://dbsp-drp.readthedocs.io/en/stable/index.html>

Table 2 shows all data acquired for the four CV candidates. Single spectra were taken at a time for each object (no coadds), with typical exposure times of 600 seconds for Keck I/LRIS and 900 seconds for P200/DBSP.

Figure 4 shows *Chandra* X-ray images and optical images from Pan-STARRS (Chambers et al. 2016) of the same sky region for four spectroscopically confirmed CVs in our sample. Figures 5 – 8 show the optical spectra of these sources. We identified prominent emission lines and computed their equivalent



**Fig. 2.** ZTF long-term (left) and phase-folded (right) light curves for 2CXO J173118.6+224248 (top panel) and 2CXO J185603.2+021259 (bottom panel) in *g* (blue) and *r* (red) filters.



**Fig. 3.** *Gaia* long-term light curves in G band for two sources in our sample. *Panels:* 2CXO J063805.1–801854 (left) and 2CXO J165219.0–441401 (right).

widths (EWs) by fitting Gaussian profiles to them. Table 3 shows the EWs of selected lines and the  $\text{HeII}(4686) / \text{H}\beta$  ratio<sup>6</sup>.

We conducted an extensive cross-match analysis between our 14 objects and publicly available optical data from the Sloan Digital Sky Survey (SDSS) and the Dark Energy Spectroscopic Instrument (DESI) collaboration (DESI Collaboration et al. 2016). With 2'' search radius, we found no matches between SDSS/APOGEE catalogs (APOGEE DR17 StarHorse VAC, Queiroz et al. (2020); APOGEE DR17 astroNN VAC, Mackereth et al. (2019); APOGEE DR17 DistMass VAC, Stone-Martinez et al. (2024); APOGEE Net VAC Sprague et al. (2022); MaStar Stellar Parameters VAC, Lazarz et al. (2022)) and our CV sample. We cross-matched our objects with the early data release (EDR) of DESI collaboration (DESI Collaboration et al. 2023), which contains spectra of more than approximately 1 million objects (DESI Collaboration et al. 2023). We found no identification of our objects with this catalog.

<sup>6</sup> 2CXO J044048.3+292434 was observed twice, and both observations show equivalent width measurements which are in agreement to within  $1\sigma$ . Therefore, in Table 3, we only report the values from the first exposure.

#### 4.2. X-ray spectra and luminosities

For each of the 14 sources in our sample, we queried the archival *Chandra* data using the observation identifier (obsid) from source observation summary results in the CSCview application<sup>7</sup>. For some objects, we additionally searched for new *Chandra* observations within a 10' search radius using the Chaser<sup>8</sup> webtool and included them in our analysis. The *Chandra* archival observations were processed by following standard *Chandra* Interactive Analysis of Observations (CIAO) (Fruscione et al. 2006) threads<sup>9</sup> (CIAO version 4.16.0 and CALDB version 4.11.0). The *chandra\_repro* tool was used to perform the initial calibration, reprocess the data, and create a level 2 event file. To extract the source and background spectra, we used the *specextract* tool in CIAO. A point-source aperture correction was applied for each source spectra by setting the parameter *correctpsf=yes*. We computed the radii of the *Chandra* point spread function (PSF) from the PSF map, which was constructed with *mkpsfmap* tool for 90% of encircled counts fraction (ECF) and

<sup>7</sup> <https://cxc.cfa.harvard.edu/csc2.0/gui/intro.html>

<sup>8</sup> <https://cda.harvard.edu/chaser/>

<sup>9</sup> <http://cxc.harvard.edu/ciao/index.html>

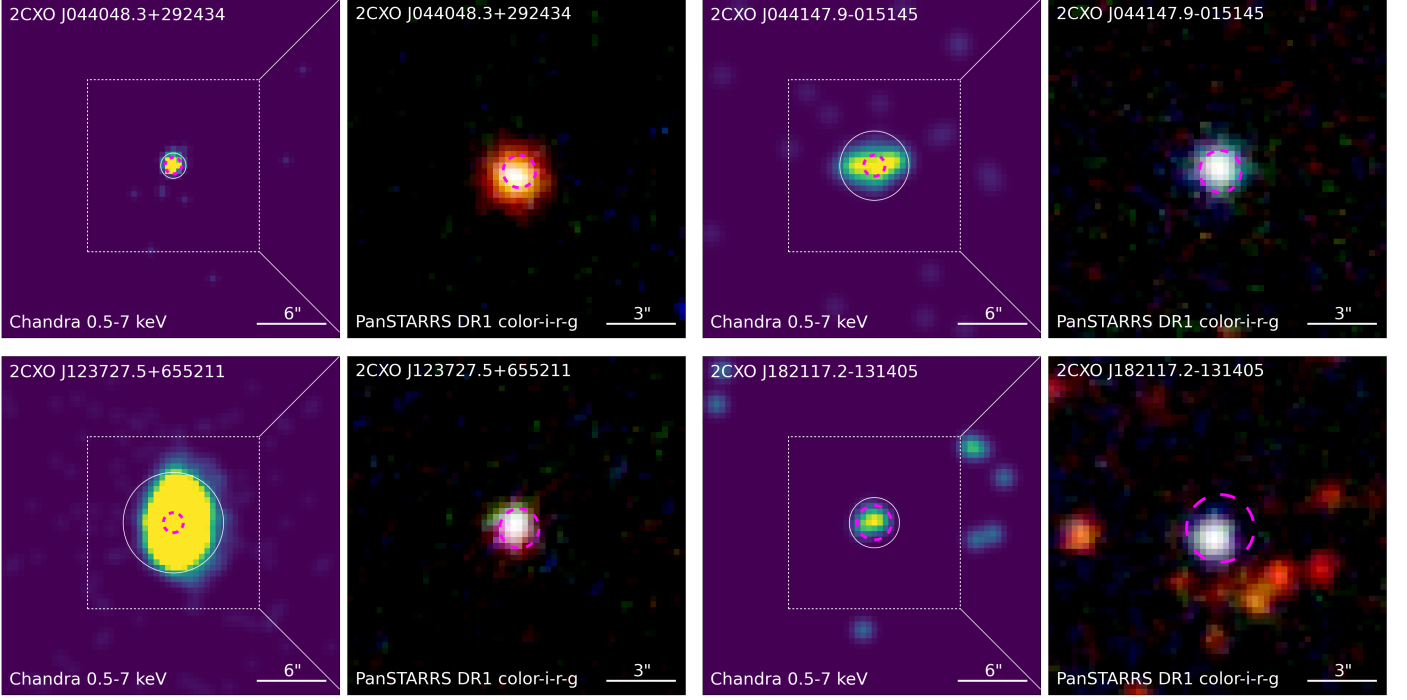


**Fig. 4.** X-ray and optical images for four new spectroscopically confirmed CVs from CSC2–*Gaia* DR3 catalog. *Left:* False-color *Chandra* X-ray images in the 0.5–7 keV energy band. The images were smoothed using a Gaussian kernel with different widths equal to 1 – 3 times the PSF radius, depending on the source counts. *Right:* Composite optical images based on Pan-STARRS color i-r-g data. *The white boxes* show the field of view of the optical images on the right. *Circles:* a PSF radius equal to the 90% of encircled counts fraction (solid, white color), and a radius equal to the major semi-axis of the error ellipse (95% localization error) centered on the source X-ray position (dashed, magenta color).

**Table 3.** Equivalent widths ( $-EW(\text{\AA})$ ) of selected lines of four spectroscopically confirmed CVs.  $3\sigma$  upper limits are shown if no higher significant measurement is detected.

Object ID (2CXO)	J044048.3+292434	J044147.9-015145	J123727.5+655211	J182117.2-131405
<i>Line (<math>\text{\AA}</math>)</i>				
<i>Emission features</i>				
H $\alpha$ 6562.8	$179 \pm 8$	$435 \pm 2$	$282 \pm 10$	$16 \pm 1$
H $\beta$ 4861.3	$95 \pm 3$	$239 \pm 3$	$397 \pm 7$	$< 20$
H $\gamma$ 4340.5	$62 \pm 3$	$139 \pm 4$	$354 \pm 8$	$< 10$
He I 5876.5	$27 \pm 6$	$64 \pm 2$	$107 \pm 9$	$< 12$
He I 7065.2	$13 \pm 3$	$15 \pm 2$	$35 \pm 9$	$8 \pm 2$
He II 4685.7	$61 \pm 4$	$< 12$	$147 \pm 7$	$< 8$
He II / H $\beta$	$0.64 \pm 0.05$	$< 0.05$	$0.37 \pm 0.02$	–

**Table 4.** List of CV candidates used to search for X-ray periodic signals.

Object ID (2CXO)	ObsID	Bin time (s)	Period (s)	PF (%)
(1)	(2)	(3)	(4)	(5)
J063805-801854	14925	1,000	$13,221 \pm 140$	61
J123727+655211	20443	1,000	–	–
J173332.5-181735	12944	200	–	–

**Notes.** (1) Source name from CSC2; (2) *Chandra* observation identification number; (3) Bin time for X-ray light-curve; (4) Period and its error found in the *Chandra* data; (5) Pulse fraction. For more details, see Section 4.3.

the 2.3 keV energy (parameters  $ecf=0.9$  and  $energy=2.3$  respectively). Source and background regions were centered at source positions from CSC2. The circle with the radius equal to the

*Chandra* PSF radius was used for the source regions, and annuli with the inner and outer radii equal to two and four times the *Chandra* PSF radius were used for background regions.

We performed the spectral fit using the XSPEC v12.13 package (Arnaud 1996) in the 0.5–7 keV energy band. We binned the X-ray spectra to have at least three counts per bin and used C-statistics (Cash 1979) to get best-fit results. We used the `error` command in XSPEC to compute  $1\sigma$  confidence intervals for the parameters. For some sources in our sample, we estimated only the  $1\sigma$  lower limit (or upper limit) of the parameters. Each spectrum was approximated using two spectral models: the power-law model (`powerlaw` in XSPEC) and the optically thin thermal plasma emission model (`mekal` in XSPEC). To take into account interstellar absorption, we used the Tuebingen-Boulder ISM absorption model (`tbabs` in XSPEC) and the solar elemental abundances from Wilms et al. (2000).

All sources in our sample are located at different distances, leading to various Galactic hydrogen column densities. We com-

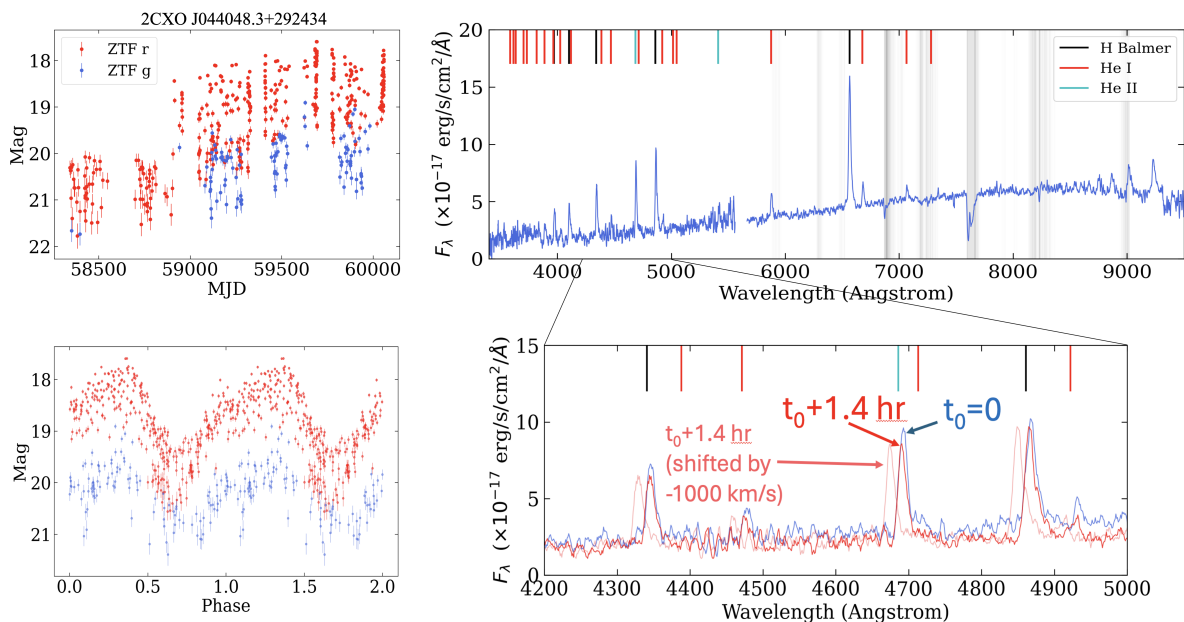


**Fig. 5.** ZTF long-term (top left) and phase-folded (bottom left) light curves in  $g$  and  $r$  filters and the DBSP optical spectrum of 2CXO J044048.3+292434 (right). *Grey lines* represent the Keck Telluric Line List. The optical spectrum (top right) shows Hydrogen Balmer and Helium emission lines and high-excitation He II 4686Å emission line, giving a high line ratio  $\text{HeII}/\text{H}\beta \approx 0.64$  (see Table 3). Optical and X-ray properties indicate that the object is a polar. Bottom right panel: Since two spectra taken 1.4 hr apart do not show a significant radial velocity shift (a  $\approx 1000$  km/s shift would be expected if this were half of the orbital period and the system were viewed edge-on), the 1.3 hr period is preferable. However, time-resolved spectroscopy for 2.6 hr would be the only way to confirm the orbital period of this system, leading us to currently label the orbital period as either 1.3 or 2.6 hr (see Section 5.1.1 for more details).

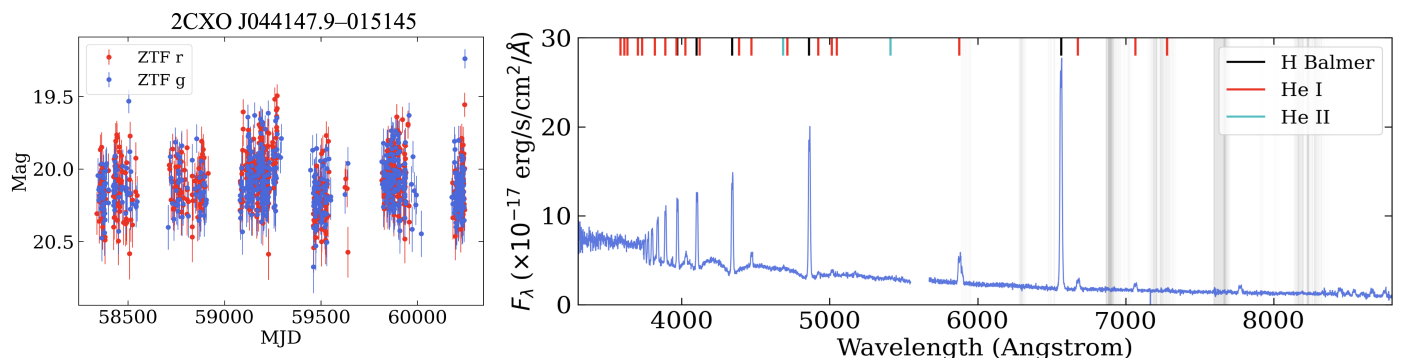


**Fig. 6.** ZTF long-term light curves in  $g$  and  $r$  filters (left) and DBSP optical spectrum of 2CXO J044147.9-015145 (right). *Grey lines* represent the Keck Telluric Line List. The optical spectrum shows WD Balmer absorption lines with no sign of the donor signature, weakly double-peaked Hydrogen and Helium emission lines, and no detectable He II 4686Å emission line, giving a  $3\sigma$  upper limit for the line ratio  $\text{HeII}/\text{H}\beta < 0.05$  (see Table 3). Optical and X-ray properties suggest that the object is a CV (WZ Sge type) (see Section 5.1.2 for more details).

puted the distances of the sources from *Gaia* parallaxes, and their errors were calculated using the standard error propagation. Using the source distances, we adopted the  $E(B-V)$  values from the Bayestar dust map (Green et al. 2019). If data from the Bayestar dust map were not available, we utilized the Galactic plane reddening map (Chen et al. 2019). We computed the hydrogen column density by assuming Cardelli’s extinction law ( $R_V \approx 3.1$ ) and the relation  $N_{\text{H}(\text{map})} \approx R_V \times E(B-V) \times 2.21 \times 10^{21} \text{ cm}^{-2}$  (Cardelli et al. 1989; Güver & Özel 2009). For sources having more than 100 counts in their X-ray spectra, we computed hydrogen column density ( $N_{\text{H}(\text{fit})}$ ) and metal abundance directly from the fit. We found no significant deviation between the best-fit results of  $N_{\text{H}(\text{fit})}$  and  $N_{\text{H}(\text{map})}$  computed from the Bayestar dust map. For other sources, we approximated their spectra with a fixed  $N_{\text{H}(\text{map})}$  and assuming solar metallicity. In the cases when  $N_{\text{H}(\text{map})}$  was not available at the specified distance of the source

or when the distance fell outside the interval classified as reliable, we fixed the hydrogen column density to the Galactic value (HI4PI Collaboration et al. 2016).

The best-fit results obtained from approximating the X-ray spectra with `powerlaw` and `mekal` models are presented in Appendix C (see Table C.1 and Figure C.1). For sources with more than one *Chandra* observation, we analyzed the X-ray spectra for each observation separately. However, we found no significant parameter variations between these separate observations subsequently performed a joint fit of the spectra in XSPEC by combining the parameters across multiple observations. We computed absorption corrected fluxes in the 0.5–7 keV energy band for the power-law model using the `cflux` command and converted them to luminosities. The approximate errors of the unabsorbed X-ray luminosities were computed from the uncertainties in the distances and fluxes using standard error propagation. Table 1

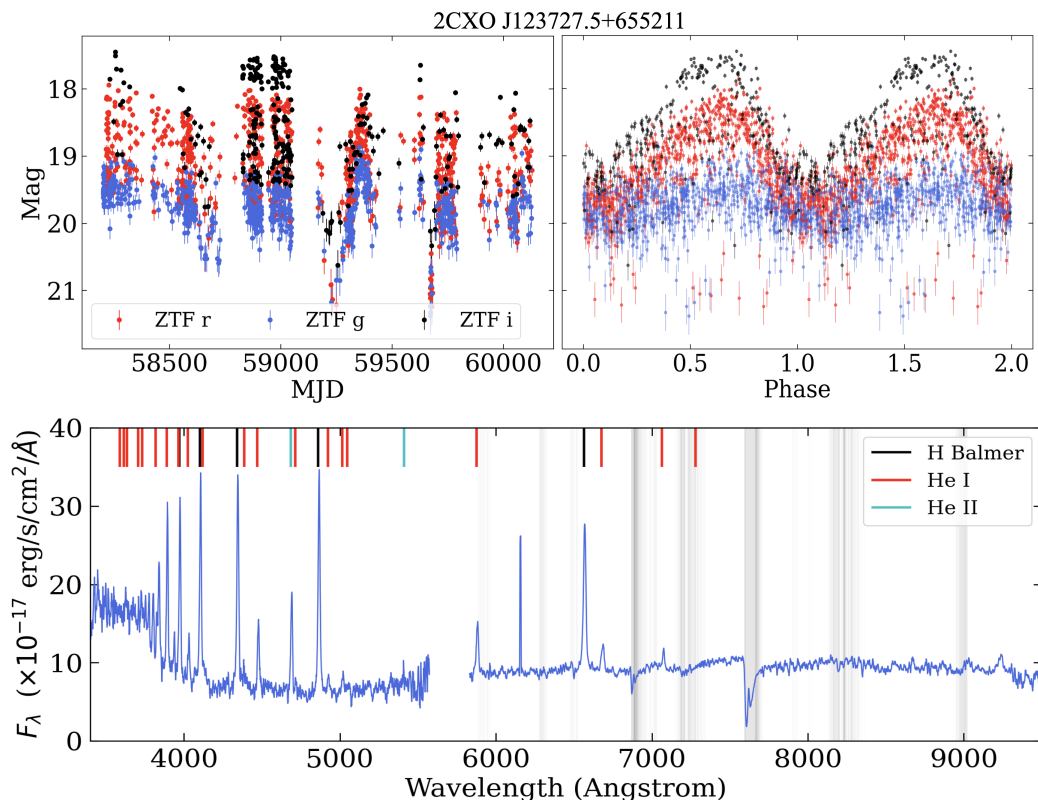


**Fig. 7.** ZTF long-term (top left) and phase-folded (top right) light curves in  $g$ ,  $r$  and  $i$  filters and the DBSP optical spectrum of 2CXO J123727.5+655211 (bottom). *Grey lines* represent the Keck Telluric Line List. The optical spectrum shows Hydrogen, Helium, and high excitation He II 4686Å emission lines, giving a line ratio of HeII /H $\beta$   $\approx$  0.37 (see Table 3). Together with optical light curves, this indicates that the object is a polar (see Section 5.1.3 for more details).

(columns 10 and 11) shows the distances and unabsorbed X-ray luminosities in the 0.5–7 keV energy band.

#### 4.3. X-ray variability and timing analysis

We searched our sample of 14 CV candidates for X-ray variable sources using the CSC2 variability indices in the 0.5–7 keV energy band:  $\text{var\_intra\_index\_b} \geq 8$  (variability within a single observation) and/or  $\text{var\_inter\_index\_b} \geq 8$  (variability across multiple observations). We found only one source matching these criteria (2CXO J063805.1–801854). We also checked the significance of the difference between the maximum and minimum fluxes between observations using the ratio  $R = (F_{\text{max}} - F_{\text{min}}) / (\sigma_{F_{\text{max}}}^2 + \sigma_{F_{\text{min}}}^2)^{1/2}$  and found only one source having  $R \geq 3$  (2CXO J123727.5+655211).

Out of the 14 CV candidates in our sample, we performed an X-ray timing analysis for three sources with more than 300 source counts in their spectra (see Table 4). If sources had more than one archival *Chandra* observation, we used the observation with the longest exposure time for the timing analysis. We extracted the background-subtracted X-ray light curves with the *dmextract* tool in CIAO, using the same source and background regions as those used for the X-ray spectral analysis. Barycentric corrections were applied for the event files by using *axbary* tool in CIAO. We used the XRONOS sub-package in FTOOLS<sup>10</sup> for timing analysis (Nasa High Energy Astrophysics Science Archive Research Center (Heasarc) 2014). First, we calculated the power spectrum density using a Fast Fourier Transform (*powspec* command in the XRONOS package) to search for peri-

odic signal. The epoch-folding (EF) technique was then applied to constrain the period of the sources (Larsson 1996) using the *efsearch* command in the XRONOS package. We estimated the best-fit period from the EF method by fitting a Gaussian function to the  $\chi^2$  vs period diagram. The period error was estimated using the bootstrap technique similarly as described in Boldin et al. (2013). To determine the significance of the detected period, we generated 1000 random Poisson, non-periodic light curves with mean source count rates and applied the *powspec* and *efsearch* tools on these randomly generated light curves. We computed the maximum value of the power spectrum density and the  $\chi^2$  (as defined in the EF method) for each generated light curve. A  $3\sigma$  upper confidence level was calculated for the distributions of power spectrum densities and  $\chi^2$  values. A strong signal was considered present in the observed X-ray light curves if the results from the *powspec* and *efsearch* tools exceeded the  $3\sigma$  confidence level determined from the simulations. We then used the *efold* tool to construct X-ray light-curves folded with the best-fit periods.

We found strong periodic X-ray signals only in one source out of three (see Table 4). Figure 9 shows the X-ray pulse profile normalized by the mean count rate of that source. The pulse fraction (PF) was computed using maximum and minimum count rates, where  $\text{PF} = (F_{\text{max}} - F_{\text{min}}) / (F_{\text{max}} + F_{\text{min}})$ . We discuss the nature of the X-ray periodic source in Section 5.2.

<sup>10</sup> <http://heasarc.gsfc.nasa.gov/ftools>

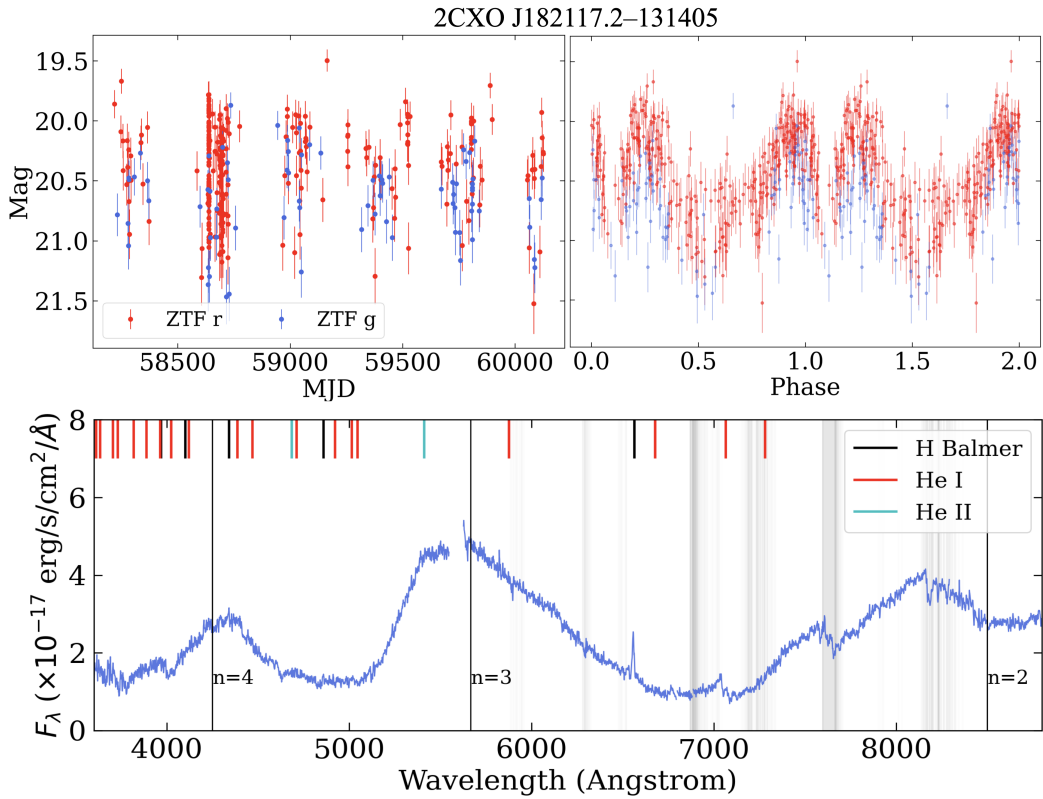


**Fig. 8.** ZTF long-term (top left) and phase-folded (top right) light curves in  $g$  and  $r$  filters and the DBSP optical spectrum of 2CXO J182117.2-131405 (bottom). *Grey lines* represent the Keck Telluric Line List. The optical spectrum is dominated by broad humps which correspond to cyclotron harmonics, and no significant  $H\beta$  and He II 4686Å emission lines are detected. A combination of the cyclotron wavelengths seen in the spectrum and the large beaming amplitude constrains the magnetic field to be  $B \approx 54 - 63$  MG. Optical and X-ray properties suggest that the object is a low accretion rate polar (see Section 5.1.4 for more details).

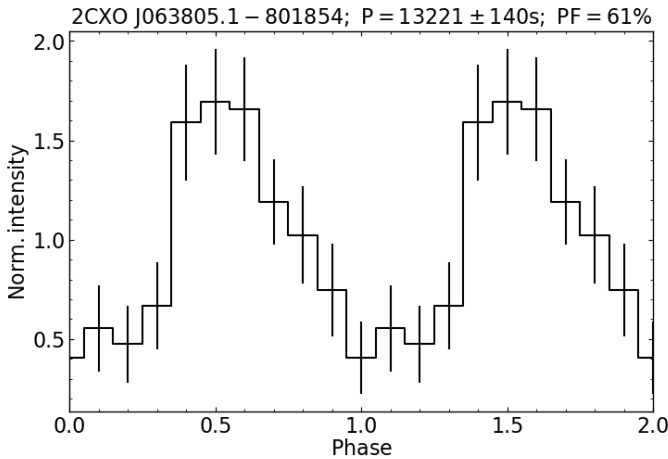


**Fig. 9.** *Chandra* X-ray pulse profile for 2CXO J063805–801854 normalized by mean count rate  $0.01 \text{ cnt s}^{-1}$ .

#### 4.4. Hertzsprung–Russell and X-ray luminosity – orbital period diagrams

To compute extinction-corrected absolute G band magnitudes for CV candidates, we directly adopted the interstellar extinction  $A_G$  (at 6000 Å) from Bayestar or the Galactic plane reddening maps when available. Otherwise, we converted the hydrogen column densities presented in Table C.1 for the *mekal* model (see Section 4.2) to interstellar extinction  $A_G$  using the Cardelli et al. (1989) extinction function. Figure 10 shows the location of the

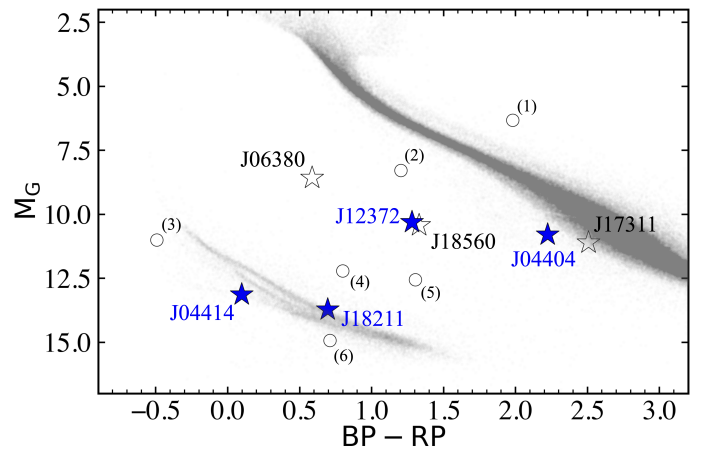


**Fig. 10.** Extinction-corrected Hertzsprung–Russell (HR) diagram. All *Gaia* sources within 100 pc with significantly measured parallaxes ( $\text{parallax\_over\_error} > 3$ ) are shown in *grey* (Gaia Collaboration et al. 2023). *Star symbols* represent new, spectroscopically confirmed CVs (blue) and variable CV candidates (white) from Table 1. *White circles* indicate CV candidates selected by a  $F_x/F_{\text{opt}}$  ratio and *Gaia* (BP-RP) color: (1) J165219.0-441401; (2) J173332.5-181735; (3) J094607.7-311550; (4) J155926.5-754311; (5) J190823.2+343328; (6) J173555.3-292530.

CV candidates on the Hertzsprung–Russell (HR) diagram along with *Gaia* objects within 100 pc that have significantly measured parallaxes ( $\text{parallax\_over\_error} > 3$ ).

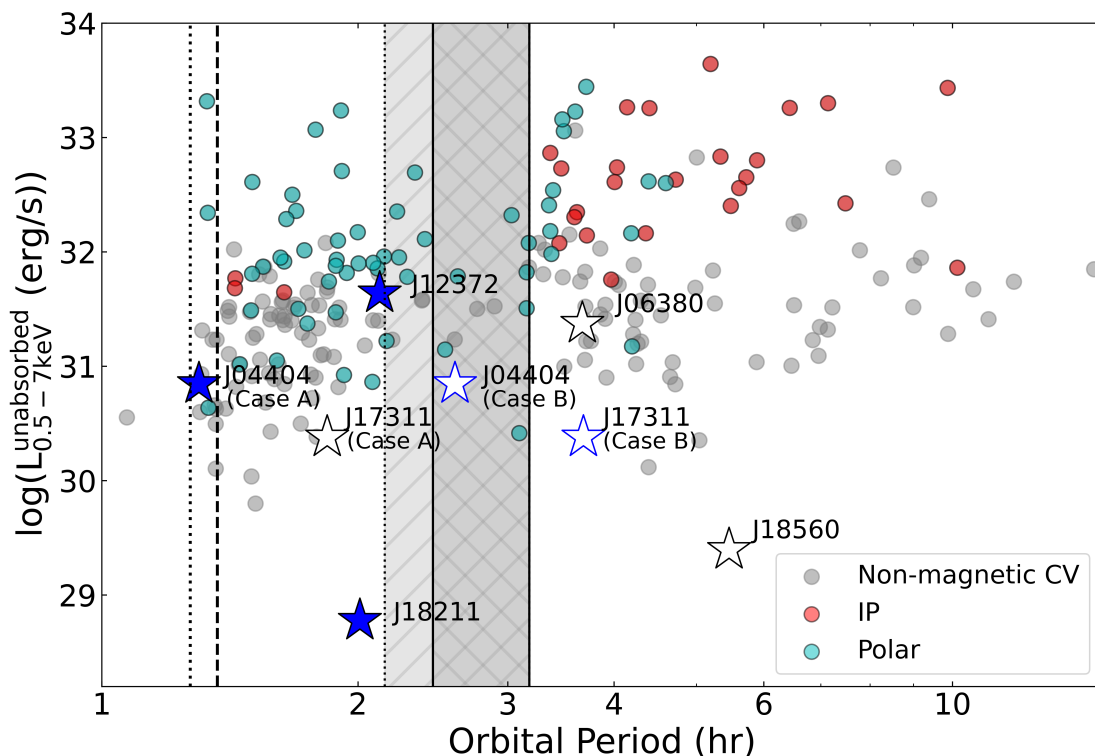


**Fig. 11.** Absorption-corrected X-ray luminosity (0.5–7 keV) – orbital period diagram for known CVs from the Ritter & Kolb (2003) catalog. X-ray luminosities were computed from fluxes in the ROSAT source catalog (2RXS) and distances in *Gaia* DR3. Circles represent known IP (red), polars (green), and non-magnetic CVs (grey). Vertical lines indicate the period minimum for CVs from: Gänsicke et al. (2009) ( $\approx 82$  min, dashed line); and Knigge (2006) ( $\approx 76$  min, dotted line). Grey shaded regions show the CV orbital period gap from: Schreiber et al. (2024) ( $\approx 2.5 - 3.2$  hr); and Knigge (2006) ( $\approx 2.2 - 3.2$  hr). Star symbols denote new, spectroscopically confirmed CVs (blue) and their candidates (white) from Table 1. We present two cases (Case A and Case B) for 2CXO J044048.3+292434 and 2CXO J173118.6+224248, as we cannot distinguish between the two orbital periods with our current data. For more details, see Section 5.

We constructed an X-ray luminosity – orbital period diagram for six objects in our sample with periods computed from the optical and X-ray data (see Figure 11). To compare our objects with other known CVs, we cross-matched the CV catalog of *Ritter and Kolb* (Final Edition, frozen on 31 December 2015, Ritter & Kolb (2003)) with the *the second ROSAT all-sky survey (2RXS) catalogue* (Boller et al. 2016), keeping only sources with a single match within  $20''$ . We then cross-matched with *Gaia* DR3 (Gaia Collaboration et al. 2023), keeping only sources with significant parallaxes and proper motions ( $5\sigma$ ), which yielded 259 sources. Next, we used the WebPimms<sup>11</sup> tool to convert ROSAT source count rates (0.1–2.4 keV) to unabsorbed X-ray luminosities in the 0.5–7 keV energy band, assuming a power-law model with a photon index of 1.7 and hydrogen column density of  $3 \times 10^{20} \text{ cm}^{-2}$ . To show different CV types in Figure 11, we used the classification scheme of the Ritter and Kolb catalog, which categorizes them as into polar (AM), intermediate polar (DQ), or otherwise as non-magnetic. In Figure 11, we show different period minimum values for CVs from Gänsicke et al. (2009) ( $\approx 82$  min) and Knigge (2006) ( $\approx 76$  min) as well as CV orbital period gap values from Schreiber et al. (2024) ( $\approx 2.5 - 3.2$  hr) and Knigge (2006) ( $\approx 2.2 - 3.2$  hr).

## 5. Results and Discussion

Table 1 shows the parameters of the 14 CV candidates found in the CSC2–*Gaia* DR3 catalog using the  $F_x/F_{\text{opt}}$  and the *Gaia* BP–RP color diagram and the period search with ZTF optical photometry (see Section 3). Figure 10 shows that most of our CV candidates are located between the main sequence and the WD regions, which is consistent with the distribution of known CVs in the *Gaia* HR diagram (e.g., Abril et al. 2020). The X-ray luminosities of all our objects vary in the  $\approx 10^{29} - 10^{32} \text{ erg s}^{-1}$  range, which matches with the range of X-ray luminosities of some known CVs (see Figure 11). X-ray spectra of our CV candidates can be approximated by a power-law model with photon indices in the  $\Gamma \approx 1 - 3$  range (or  $kT \sim 1 - 70$  keV for the optically thin thermal emission model). Such X-ray spectra are seen in some magnetic and non-magnetic CVs (e.g., Galiullin & Gilfanov 2021; Schwöpe et al. 2022a,b; Rodriguez et al. 2023a; Galiullin et al. 2024).

Our variability search indicates that seven sources out of these 14 CV candidates are variable in nature. The X-ray luminosity – orbital period diagram shows that most of our variable sources have X-ray luminosities and periods typically seen for magnetic and non-magnetic CVs (see Figure 11). Only two sources (2CXO J182117.2–131405 and 2CXO J185603.2+021259) are located in a distinct region of the phase space compared to the main sample of CVs, and exhibit low X-ray luminosity. These two objects might be a low-accretion rate

<sup>11</sup> <https://heasarc.gsfc.nasa.gov/cgi-bin/Tools/w3pimms/w3pimms.pl>

CV and an eclipsing binary<sup>12</sup>. We spectroscopically confirm four objects in our sample as new CVs. Their optical spectra show prominent emission lines or cyclotron humps, features typically observed in CVs (see Figures 5 - 8). Below, we provide a detailed discussion of these CVs and other variable objects in our sample.

We note that some objects in our sample were previously suggested to be CV or quiescent low-mass X-ray binary (qLMXB) candidates using a multiwavelength machine-learning method, however, the results have low confidence (Yang et al. 2022). Objects having *Gaia* optical light curves were also classified as possible CV candidates using a machine learning variability classifier in *Gaia* DR3 (Gaia Collaboration et al. 2023). In Appendix B, we discuss three recently discovered CVs, which we independently selected using the methods described in this paper. These examples demonstrate that the  $F_X/F_{\text{opt}}$  and *Gaia* BP–RP color diagram, as suggested by Rodriguez (2024) can be a powerful method for searching and independently selecting accreting binary candidates. Without optical follow-up, it is challenging to distinguish between CVs and qLMXBs, as they display similar  $F_X/F_{\text{opt}}$  ratios and have overlapping X-ray luminosity ranges. Further spectroscopic follow-up to place constraints on the mass of the accreting object is required for the rest of the objects in our sample to clarify their nature.

### 5.1. Spectroscopically Confirmed CVs

Here, we discuss the nature of four objects from our final sample of CV candidates, for which we obtained optical spectra using Keck I/LRIS or Palomar/DBSP.

#### 5.1.1. 2CXO J044048.3+292434, a new polar

We present the optical spectrum of J044048.3+292434 (hereafter J04404) in the right panel of Figure 5. It shows Hydrogen Balmer and Helium emission lines along with a high-excitation He II 4686Å emission line, yielding a high line ratio of  $\text{HeII}/\text{H}\beta \approx 0.64$ , which is typically seen in polars (see Table 3).

J04404 shows a flux ratio of about  $F_X/F_{\text{opt}} \approx 0.6$ , and an X-ray luminosity  $L_X \approx 7.1 \times 10^{30} \text{ erg s}^{-1}$  (see Table 1). The X-ray spectrum can be approximated by a power-law model with an unusually shallow photon index  $\Gamma \approx 0.5$  (or  $kT \gtrsim 55.5 \text{ keV}$  for an optically thin thermal emission model) (see Table C.1 and Figure C.1), a characteristic observed in some magnetic CVs (e.g., Galiullin & Gilfanov 2021). J04404 is located close to the period minimum of CVs in the X-ray luminosity–period diagram (see Figure 11). Its optical and X-ray properties indicate that J04404 is a polar near the CV period minimum.

In the left panels of Figure 5, we present the long-term ZTF light curve of J04404 and the phase-folded light curve at the best period (1.30 h = 78 min). It is evident that J04404 underwent a state change, commonly observed in polars, around MJD = 59000, where the average optical *r* filter magnitude increased from  $r \sim 21$  to  $r \sim 19$  (see top left panel of Figure 5).

In some cases, polars can show two peaks in their optical light curve within a single orbital period due to cyclotron beam-

ing<sup>13</sup>. The phase-folded optical light curve of J04404 shows  $\sim 2$  mag peak-to-peak modulation, which is characteristic of cyclotron beaming following a state change in polars (see the bottom left panel of Figure 5). In order to determine if the orbital period of J04404 is 1.30 hr or 2.60 hr, we utilized the fact that the Hydrogen Balmer and He II emission lines in polars typically vary by  $\approx 1000 \text{ km/s}$  within a single orbital period (e.g., Rodriguez et al. 2023b). In the case of J04404, two spectra taken 1.4 hr apart do not show a significant radial velocity shift. In the bottom right panel of Figure 5, we show both spectra of J04404, taken 1.4 hr apart. We also show a  $\approx 1000 \text{ km/s}$  shift, which would be expected if 1.4 hr were approximately half of the orbital period. However, we note that if the system were viewed nearly perpendicular to the accretion stream, such a radial velocity shift would not be observed. Time-resolved spectroscopy for 2.6 hr is necessary to confirm the orbital period of this system, leading us to currently label the orbital period as either 1.3 or 2.6 hr.

#### 5.1.2. 2CXO J044147.9-015145, a low accretion rate non-magnetic CV

In Figure 6 (left panel), we present the long-term ZTF optical light curve of 2CXO J044147.9-015145 (hereafter J04414). A preliminary Lomb-Scargle period analysis reveals no periodicity in the ZTF data, indicating that further data are required to determine the possible orbital period of this system. The optical spectrum of J04414 is shown in Figure 6 (right panel). Hydrogen and Helium emission lines are present, with no detectable He II 4686Å emission line, giving a  $3\sigma$  upper limit for the line ratio  $\text{HeII}/\text{H}\beta < 0.05$  (see Table 3). J04414 shows a flux ratio of  $F_X/F_{\text{opt}} \approx 0.3$  and an X-ray luminosity  $L_X \approx 3.1 \times 10^{29} \text{ erg s}^{-1}$ . The X-ray spectrum can be approximated by a power-law model with a photon index  $\Gamma \approx 1.8$  (or  $kT \approx 4.5 \text{ keV}$  for an optically thin thermal emission model) (see Table C.1 and Figure C.1). The optical and X-ray properties suggest that J04414 is a low accretion rate non-magnetic CV (WZ Sge type). This classification is based on the apparent WD Balmer absorption lines and weakly double-peaked central emission lines seen in the center of its optical spectrum. There is no sign of the donor signature in the optical spectrum. The *Gaia* HR diagram (see Figure 10) also supports this classification, as J04414 is located in the WD region, where WZ Sge type systems are concentrated (e.g., Abril et al. 2020).

#### 5.1.3. 2CXO J123727.5+655211, a new polar

In Figure 7 (top panels), we present the long-term ZTF light curve and the phase-folded light curve at the best period for 2CXO J123727.5+655211 (hereafter J12372). The ZTF light curve reveals a significant period at 2.12 hr. The color dependence of cyclotron beaming is evident, with the ZTF *i* filter showing the highest modulation (peak-to-peak  $\sim 2$  mag) and the ZTF *g* filter showing the lowest (peak-to-peak  $\sim 1$  mag) (see the top left panel of Figure 7).

We present the optical spectrum of J12372 in Figure 7 (bottom panel). The spectrum shows Hydrogen, Helium, and high

<sup>12</sup> Such a binary would be an “active binary”, like RS CVn systems, which have orbital periods from as low as 5–6 hours to  $\sim 10$  days. In these systems, X-rays originate from the hot corona of one or both stellar components (e.g. Walter & Bowyer 1981).

<sup>13</sup> A two-component cyclotron model has been used to model the optical and near-infrared light curves of polars, such as in Campbell et al. (2008). A two-component cyclotron model leads to two peaks in a single orbital period, and can be due to any of the following: two magnetic poles of different field strength, optical depth, and/or viewing angles.

excitation He II 4686Å emission lines, yielding a line ratio of  $\text{HeII}/\text{H}\beta \approx 0.37$  (see Table 3).

J12372 shows a flux ratio  $F_X/F_{\text{opt}} \approx 1.1$  and an X-ray luminosity  $L_X \approx 4.4 \times 10^{31} \text{ erg s}^{-1}$  (see Table 1). The X-ray spectrum can be approximated by a power-law model with a photon index  $\Gamma \approx 1.4$  (or  $kT \approx 38.3 \text{ keV}$  for an optically thin thermal emission model) (see Table C.1 and Figure C.1). X-ray timing analysis revealed no significant period in the longest exposure *Chandra* observation (see Table 4). J12372 shows significant X-ray flux variability ( $R \approx 6$ , see Section 4.3), with a factor of  $\approx 2$  between the *Chandra* observations, but no statistically significant variability between the spectral parameters was found. J12372 lies close to the CV period gap in the X-ray luminosity–period diagram (see Figure 11). Together with the optical light curves and spectrum, this indicates that J12372 is a polar.

#### 5.1.4. 2CXO J182117.2–131405, low accretion rate polar

Figure 8 (top panels) shows the optical long-term ZTF light curve of 2CXO J182117.2–131405 (hereafter J18211) and the phase folded light curve. We determined its best period to be 2.01 hr using the Lomb-Scargle period analysis. The phase-folded optical light curve shows cyclotron beaming near phase 0.15 and  $\approx 1 \text{ mag}$  peak-to-peak modulation (see top right panel of Figure 8). This modulation could be either due to cyclotron beaming or an eclipse of the WD by the donor star. High-speed photometry is needed to further investigate these scenarios.

J18211 has a low number of X-ray counts, and its spectrum can be approximately fitted by a power-law model, resulting in a large uncertainty for a photon index  $\Gamma \sim 1.7$  (or  $kT \gtrsim 1.6 \text{ keV}$  for an optically thin thermal emission model) (see Table C.1 and Figure C.1). J18211 shows a flux ratio  $F_X/F_{\text{opt}} \approx 0.15$  and a lower X-ray luminosity ( $L_X \approx 6 \times 10^{28} \text{ erg s}^{-1}$ ) than typically seen in CVs (see Table 1). J18211 is located near the edge of the CV period gap in the X-ray luminosity–period diagram (see Figure 11). In this part of the diagram, the canonical picture of CV evolution predicts that detached systems begin to undergo accretion again. Hence, J18211 could be a low accretion rate polar (previously referred to as a pre-polar).

We present the optical spectrum of J18211 in Figure 8 (bottom panel). The spectrum is dominated by broad humps corresponding to cyclotron harmonics with no significant  $\text{H}\beta$  and He II 4686Å emission lines detected. Using the equation for the electron gyration frequency around a magnetic field, we can define the wavelength of cyclotron harmonics as the following:

$$\lambda_n = \frac{10710}{n} \left( \frac{100 \text{ MG}}{B} \right) \sin \theta \text{ \AA} \quad (2)$$

With the spacing of two harmonics, it is possible to constrain the magnetic field strength, as the spacing must always be the ratio of integers. We must assume a cyclotron beaming angle, which should be close to  $90^\circ$  since the amplitude of the cyclotron harmonics is so large (An angle  $\theta > 60^\circ$  is a good approximation for cyclotron beaming factors greater than 2 (e.g. Campbell et al. 2008)). Detailed cyclotron modeling is beyond the scope of this paper. In this work, we fixed the magnetic field at different values and approximately matched the location of the cyclotron humps in the spectrum to different cyclotron harmonics (see Figure 8). This combination of the cyclotron wavelengths observed in the spectrum of J18211 and the large beaming amplitude constrains the magnetic field to be  $B \approx 54 - 63 \text{ MG}$ . This magnetic field strength is typical of low accretion rate polars (e.g., Parsons et al. 2021).

## 5.2. Variable CV candidates

Here, we discuss four CV candidates classified based on their X-ray and optical variability, but for which optical spectra are not yet available.

### 5.2.1. 2CXO J063805.1–801854: A magnetic CV?

2CXO J063805.1–801854 (hereafter J06380) shows  $F_X/F_{\text{opt}} \approx 0.8$  and X-ray luminosity  $L_X \approx 2.4 \times 10^{31} \text{ erg s}^{-1}$  (see Table 1). Its spectrum can be approximated by a power-law model with an unusually shallow photon index  $\Gamma \approx 0.2$  (or  $kT \gtrsim 75 \text{ keV}$  for an optically thin thermal emission model) (see Table C.1 and Figure C.1). Such a shallow photon index is observed in the X-ray spectra of some magnetic CVs, such as polars or IPs (e.g., Galiullin & Gilfanov 2021). X-ray timing analysis revealed a  $\approx 13,200 \text{ sec}$  periodicity (PF = 61%), which is consistent with the period previously found by Israel et al. (2016) in the same *Chandra* data (see Table 4 and Figure 9). There is no available optical ZTF photometry for J06380. The *Gaia* optical light curve shows an outbursting-type variability with  $\approx 3 \text{ mag}$  outburst lasting around  $\approx 100 \text{ days}$  and a possible recurrence time of approximately  $\approx 500 \text{ days}$  (see Figure 3). Figure 11 shows that J06380 lies within main sample of known CVs. The X-ray periodicity (in the range of CV orbital periods), along with a high X-ray luminosity and hard spectrum, suggests that J06380 could be a magnetic CV, likely an IP.

### 5.2.2. 2CXO J165219.0–441401: A possible dwarf nova?

2CXO J165219.0–441401 (hereafter J16521) shows  $F_X/F_{\text{opt}} \approx 1.2$  and a high X-ray luminosity  $L_X \approx 3 \times 10^{32} \text{ erg s}^{-1}$  (see Table 1). The X-ray spectrum can be approximated by a power-law model with a photon index  $\Gamma \approx 1.5$  (or  $kT \approx 5.8 \text{ keV}$  for an optically thin thermal emission model) (see Table C.1 and Figure C.1). There is no ZTF photometry for J16521 and the *Gaia* optical light curve shows a  $\approx 3 \text{ mag}$  outburst with a possible  $\approx 500 \text{ days}$  recurrent time (see Figure 3). This suggests that J16521 could be a dwarf nova.

### 5.2.3. 2CXO J173118.6+224248: A possible non-magnetic CV?

2CXO J173118.6+224248 (hereafter J17311) shows  $F_X/F_{\text{opt}} \approx 0.3$  and an X-ray luminosity  $L_X \approx 2.4 \times 10^{30} \text{ erg s}^{-1}$  (see Table 1). The optical ZTF light curves show  $\approx 0.5 \text{ mag}$  variability with a period of about  $\approx 1.8 \text{ hr}$  (see Figure 2). However, the actual period may be twice this value, possibly due to ellipsoidal modulation. The X-ray spectrum can be approximated by a power-law model with a photon index  $\Gamma \approx 2.2$  (or  $kT \approx 3.0 \text{ keV}$  for an optically thin thermal emission model) (see Table C.1 and Figure C.1), a characteristic observed in non-magnetic CVs. J17311 is located close to the main sequence of known CVs in the X-ray luminosity–orbital period diagram (see Figure 11). The X-ray properties and optical variability suggest that J17311 is a non-magnetic CV.

### 5.2.4. 2CXO J185603.2+021259: A possible eclipsing binary?

2CXO J185603.2+021259 (hereafter J18560) shows  $F_X/F_{\text{opt}} \approx 0.05$  and a lower X-ray luminosity ( $L_X \approx 2.5 \times 10^{29} \text{ erg s}^{-1}$ ), than observed in CVs (see Table 1). The ZTF optical light curve

shows deep eclipses of approximately  $\approx 1$  mag in the  $r$  filter (or approximately  $\approx 1.5$  mag in the  $g$  filter) with a period of about 5.5 hr (see Figure 2). Out of the eclipse sinusoidal variability with  $\approx 0.1$  mag is seen, possibly caused by the contribution from the donor. The X-ray spectrum can be approximated by a power-law model having a photon index  $\Gamma \approx 2.8$  (or  $kT \approx 1$  keV for an optically thin thermal plasma model) (see Table C.1 and Figure C.1). Figure 11 shows that J18560 is located below the main CV sample, similar to J18211. These observed properties suggest that J18560 could be an eclipsing binary.

## 6. Conclusions

We searched for new Galactic CV candidates among 25,887 sources in the CSC2, cross-matched these with *Gaia* DR3, and studied their optical and X-ray properties. We summarize our findings below:

- We used a modern concept suggested by Rodriguez (2024) to classify new CVs among stellar objects based on a combination of  $F_X/F_{\text{opt}}$  and *Gaia* BP–RP color (so called the “X-ray Main Sequence”) (see Figure 1). We further defined a new threshold cut to compile a pure sample of CV candidates and minimize contamination from stellar objects (see Eq.1 and Section 3).
- We excluded known Galactic stellar objects by cross-matching the CSC2 – *Gaia* DR3 catalog with the Simbad database and other publicly available CV catalogs (see Section 2). Out of 13,956 unclassified Galactic objects, we identified 14 new CV candidates using two different cuts on the “X-ray Main Sequence” (see Table 1 and Section 3).
- All objects show X-ray luminosities in the range  $L_X \approx 10^{29} - 10^{32}$  erg s $^{-1}$ . Their X-ray spectra can be approximated by a power-law model with photon indices in the  $\Gamma \sim 1 - 3$  range or by an optically thin thermal emission model in the  $kT \sim 1 - 70$  keV range (see Figure C.1 and Table C.1). These X-ray properties are mostly typical of CVs (both magnetic and non-magnetic), but some objects might also be qLMXBs.
- We performed optical follow-up observations with Keck I/LRIS and P200/DBSP and spectroscopically confirmed four objects as new CVs. Their optical spectra show prominent emission lines or cyclotron humps, typically seen in CVs (see Tables 2 and 3). We determined orbital periods for three of these objects using ZTF photometry. Among these, we discovered two polars, one low accretion rate polar and one non-magnetic CV (WZ Sge type) (see Section 5.1).
- The X-ray and optical properties of four variable CV candidates suggest that three are potential magnetic systems or dwarf novae, while one may be an eclipsing binary (see Section 5.2). Further spectroscopic follow-up is required to confirm the nature of these objects.

Our analysis shows that a multiwavelength approach is a powerful tool for discovering new CVs and studying their properties. We illustrated that the “X-ray Main Sequence” presented in Rodriguez (2024) allows us to compile a sample of CV candidates for a detailed study. This approach can also be applied to other X-ray catalogs or upcoming all-sky SRG/eROSITA data

to search for accreting binary systems. Further investigation of selection effects is necessary to use the “X-ray Main Sequence” to compile volume-limited samples of CVs and study their population.

*Acknowledgements.* This research has made use of data obtained from the *Chandra* Data Archive and software provided by the *Chandra* X-ray Center (CXC) in the application packages CIAO. This research has made use of the SIMBAD database, operated at CDS, Strasbourg, France. Based on observations obtained with the Samuel Oschin Telescope 48-inch and the 60-inch Telescope at the Palomar Observatory as part of the Zwicky Transient Facility project. ZTF is supported by the National Science Foundation under Grants No. AST-1440341 and AST-2034437 and a collaboration including current partners Caltech, IPAC, the Weizmann Institute of Science, the Oskar Klein Center at Stockholm University, the University of Maryland, Deutsches Elektronen-Synchrotron and Humboldt University, the TANGO Consortium of Taiwan, the University of Wisconsin at Milwaukee, Trinity College Dublin, Lawrence Livermore National Laboratories, IN2P3, University of Warwick, Ruhr University Bochum, Northwestern University and former partners the University of Washington, Los Alamos National Laboratories, and Lawrence Berkeley National Laboratories. Operations are conducted by COO, IPAC, and UW. The ZTF forced-photometry service was funded under the Heising-Simons Foundation grant No.12540303 (PI: Graham). We are grateful to the staffs of the Palomar and Keck Observatories for their work in helping us carry out our observations. This work has made use of data from the European Space Agency (ESA) mission *Gaia* (<https://www.cosmos.esa.int/gaia>), processed by the *Gaia* Data Processing and Analysis Consortium (DPAC, <https://www.cosmos.esa.int/web/gaia/dpac/consortium>). Funding for the DPAC has been provided by national institutions, in particular the institutions participating in the *Gaia* Multilateral Agreement. This research made use of matplotlib, a Python library for publication quality graphics (Hunter 2007); NumPy (Harris et al. 2020); Astroquery (Ginsburg et al. 2019); Astropy, a community-developed core Python package for Astronomy (Astropy Collaboration et al. 2013, 2018); and the VizieR catalogue access tool, CDS, Strasbourg, France. IG, AS, VD, NT acknowledge support from Kazan Federal University. ACR acknowledges support from the National Science Foundation via an NSF Graduate Research Fellowship. The authors thank the anonymous referee for useful and inspiring suggestions which helped to improve the manuscript.

## Appendix A: General object types with a Simbad and $F_X/F_{\text{opt}} - (BP - RP)$ selection cut

Table A.1 shows our general object types based on the Simbad hierarchical structure. The columns are: (1) our main object type; (2) object sub-type; (3) title of Simbad hierarchical structure used to define the main object type and its sub-type; (4) number of sources per each object sub-type, including known sources and their candidates. No source in our sample had an object type from the sixth Simbad's hierarchy ("Gravitation"); therefore, it's not shown in Table A.1.

We investigated purity and completeness to construct a pure sample of new CV candidates and avoid contamination from stellar objects. Based on the Simbad hierarchical structure, we created two samples of known CVs (36 sources) and STARS (4781 sources) (see Section 3.1).

Smethurst et al. (2022) computed purity and completeness for the red and blue galaxies classified by optical color. We applied a similar approach to define the purity and completeness as:

- True positive (TP) = known CVs classified as CVs based on a given threshold (i.e., known CVs with an observed X-ray-to-optical ratio exceeding the threshold cut,  $(F_X/F_{\text{opt}})_{\text{obs}} \geq (F_X/F_{\text{opt}})_{\text{cut}}$ ).
- False positive (FP) = known STARS classified as CVs based on a given threshold (i.e., known STARS with an observed X-ray-to-optical ratio exceeding the threshold cut,  $(F_X/F_{\text{opt}})_{\text{obs}} \geq (F_X/F_{\text{opt}})_{\text{cut}}$ ).
- False negative (FN) = known CVs classified as STARS (i.e., known CVs with an observed X-ray-to-optical ratio below the threshold cut,  $(F_X/F_{\text{opt}})_{\text{obs}} < (F_X/F_{\text{opt}})_{\text{cut}}$ ).

Purity (P) is computed as the fraction of true identification to all identifications,

$$P = TP / (TP + FP), \quad (\text{A.1})$$

and the completeness (C) is calculated as the fraction of true detections to all that should have been classified,

$$C = TP / (TP + FN). \quad (\text{A.2})$$

To find the optimal combination of linear parameters (A, B) for Eq.1, we created a grid of parameters with the 0.1 steps in the range  $0 \lesssim A \lesssim 3$  and  $-8 \lesssim B \lesssim 3$  and computed the purity and completeness.

Figure A.1 shows the purity and completeness as a function of linear parameters (A, B). For illustrative purposes, we show the purity and completeness only for three B parameters. The  $B = 0$  case corresponds to the canonical selection cut based only on the X-ray-to-optical flux ratio without additional information from *Gaia* colors. For example, the cut  $F_X/F_{\text{opt}} = 0.1$  (where  $A = -1$  and  $B = 0$ ) gives  $\approx 27\%$  purity and  $\approx 48\%$  completeness. The drop of the purity above the  $A \gtrsim -0.2$  is caused by a low number of sources and is not statistically significant. The Rodriguez (2024) empirical cut ( $A = -3.5$  and  $B = 1$ ) shows  $\approx 25\%$  purity and  $\approx 78\%$  completeness. In our study, we chose to use  $A = -1.5$  and  $B = 0.7$ , which gives  $\approx 100\%$  purity and  $\approx 52\%$  completeness.

We note that our threshold is defined based only on a small sample of confirmed CVs (36 objects). To study the CV population and create a volume-limited sample, the  $F_X/F_{\text{opt}}$  and *Gaia* BP–RP color diagram should be further investigated for selection effects with a large sample of confirmed CVs and stellar objects. A detailed investigation is beyond the scope of this paper.

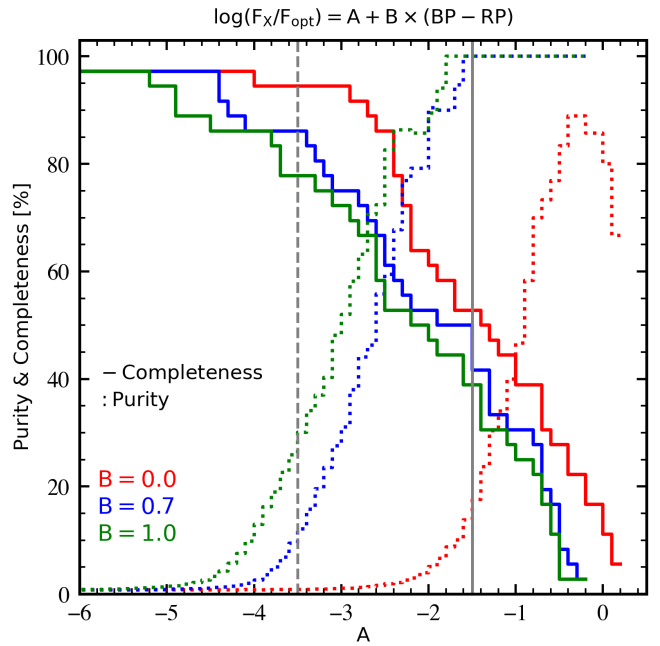


**Fig. A.1.** Purity (dotted line) and Completeness (solid line) computed for different (A, B) parameters from Eq. 1. The vertical solid line corresponds to  $A = -1.5$  (and  $B = 0.7$ ), which is used to select a pure sample of CV candidates in this paper. The vertical dashed line shows  $A = -3.5$  (and  $B = 1$ ) for an empirical cut from Rodriguez (2024).

## Appendix B: Recently discovered CVs

We selected three objects from the CSC2–*Gaia* DR3 catalog using the X-ray main sequence as CV candidates (see Figure 1 and Table B.1). In the course of this study, two of these objects (2CXO J024131.0+593630 and 2CXO J143435.3+334049) were recently discovered as CVs with SDSS spectra and ZTF light curves (Inight et al. 2023). Another object, 2CXO J174133.7–284034<sup>14</sup>, was confirmed as a CV via optical spectroscopy by Wevers et al. (2017). However, we included this object in our analyses to search for possible X-ray variability through timing and spectral analyses. Here, we individually discuss the X-ray and optical properties of these objects.

### Appendix B.1: 2CXO J024131.0+593630, a non-magnetic CV

In the left panel of Figure B.1, we present the long-term optical ZTF light curve of 2CXO J024131.0+593630 (hereafter J02413), which shows two significant ( $\approx 2$  mag in *r* filter and  $\approx 3$  mag in *g* filter) short outbursts. A preliminary Lomb-Scargle period analysis reveals no periodicity in the ZTF and *Gaia* data, indicating that further observations are needed to determine the possible orbital period of this system.

We observed J02413 with P200/DBSP on 6 December 2023 for 900s. The optical spectrum of J02413 is presented in the right panel of Figure B.1. Single-peaked Hydrogen Balmer emission lines are clearly visible, and a weak He II 4686Å emission line is also present, giving a low line ratio  $\text{HeII}/\text{H}\beta \approx 0.12$  (see Table B.2). However, as noted in Table B.2, the detection of He II 4686Å does not pass a visual inspection, so the value of the

<sup>14</sup> We included this system in our analysis because it appears as an X-ray source ("X") in Simbad, not explicitly as a CV.

**Table A.1.** Object types based on Simbad classification for 25,887 sources in the CSC2–*Gaia* DR3 catalog.

Main object type (1)	Sub-type (2)	Simbad Class (3)	N <sub>src</sub> (4)	Comments
<b>STARS</b>				
	Star	1. Taxonomy of Stars	4,779	General sub-type from Simbad database
	Massive stars	1.1 Massive Stars and their Remnants	42	
	YSO	1.2 Young Stellar Objects (Pre-Main Sequence Stars)	4,823	
	Main-sequence stars	1.3 Main Sequence Stars	37	
	Evolved	1.4 Evolved Stars	140	
	Peculiar	1.5 Chemically Peculiar Stars	15	
	Binaries	1.6 Interacting Binaries and close Common Proper Motion Systems	638	
	Low-mass stars	1.8 Low mass Stars and substellar Objects	101	
	Properties	1.9 Properties, variability, spectral kinematic or environment	476	
	Spectral properties	1.10 Spectral properties	239	
	Kinematic	1.11 Kinematic and Environment Properties	205	
	Sets of stars	2. Sets of Stars	5	
	WD	1.4 Evolved Stars	13	
	Brown dwarf (BD)	1.8 Low mass Stars and substellar Objects	4	
<b>ACCRETING BINARIES</b>				
	CV	1.6 Interacting Binaries and close Common Proper Motion Systems	32	Sub-type includes CV, Nova and Symbiotic Stars
	X-ray Binary	1.6 Interacting Binaries and close Common Proper Motion Systems and 7. General Spectral Properties	50	Sub-type includes X-ray binary (HMXB, LMXB) and ULX
<b>ISM</b>				
	ISM	3. Interstellar Medium	7	
<b>GALAXY</b>				
	Galaxy	4. Taxonomy of Galaxies	47	
	Sets of Galaxies	5. Sets of Galaxies	6	
<b>PROPERTIES</b>				
	Properties	7. General Spectral Properties	520	
<b>BLENDS</b>				
	Blends	8. Blends, Errors, not well Defined Objects	2	
<b>UNKNOWN</b>				
		–	13,706	Object is not presented in Simbad database

**Table B.1.** List of previously known CVs independently found in our search of the CSC2–*Gaia* DR3 catalog.

Object ID (2CXO)	R.A.	DEC.	R <sub>95</sub> (")	<i>Gaia</i> DR3 source_id	G (mag)	BP–RP (mag)	F <sub>X</sub> /F <sub>opt</sub>	Var.	d (pc)	L <sub>X</sub> (10 <sup>30</sup> erg s <sup>−1</sup> )	Obj. Type	Opt. Spec.
(1)	(2)	(3)	(4)	(5)	(6)	(7)	(8)	(9)	(10)	(11)	(12)	(13)
J024131.0+593630	02 41 31.1	+59 36 30.5	0.72	464373929923792384	19.84	1.47	1.71	Z/Ga	541 ± 121	14.78 ± 6.70	1	✓
J143435.3+334049	14 34 35.3	+33 40 49.5	3.72	1287753107989718784	20.03	0.23	0.30	–	343 ± 50	0.48 ± 0.16	4	✓
J174133.7–284034	17 41 33.8	−28 40 34.5	0.73	4060179580171407360	18.75	0.99	0.97	–	784 ± 161	44.12 ± 18.23	3	

**Notes.** Same notes as in Table 1. (9) "Z" –outbursting source based on ZTF photometry (see Section 3.2).

ratio should be interpreted as an upper limit. We also note that the detection (or non-detection) of He II 4686Å does not affect our final interpretation of this object.

J02413 shows a high flux ratio  $F_X/F_{opt} \approx 1.7$  and an X-ray luminosity  $L_X \approx 1.5 \times 10^{31}$  erg s<sup>−1</sup> (see Table B.1). The X-ray spectrum of J02413 can be approximated by a power-law model with  $\Gamma \approx 1.8$  (or kT  $\approx 5.5$  keV for an optically thin thermal emission model) (see Table C.1 and Figure C.1). We found no significant period for J02413 from the X-ray timing analysis of the longest exposure *Chandra* observation (ObsID = 7152).

J02413 also does not show X-ray flux variability and or changes in spectral parameters between observations. Our analysis, using optical and X-ray properties, suggests that J02413 is a CV, likely non-magnetic. This agrees with Inight et al. (2023) conclusion, where J02413 is identified as a new non-magnetic CV (U Gem type). The spectrum of this object is not shown in Inight et al. (2023), making our spectrum a useful addition to the literature.

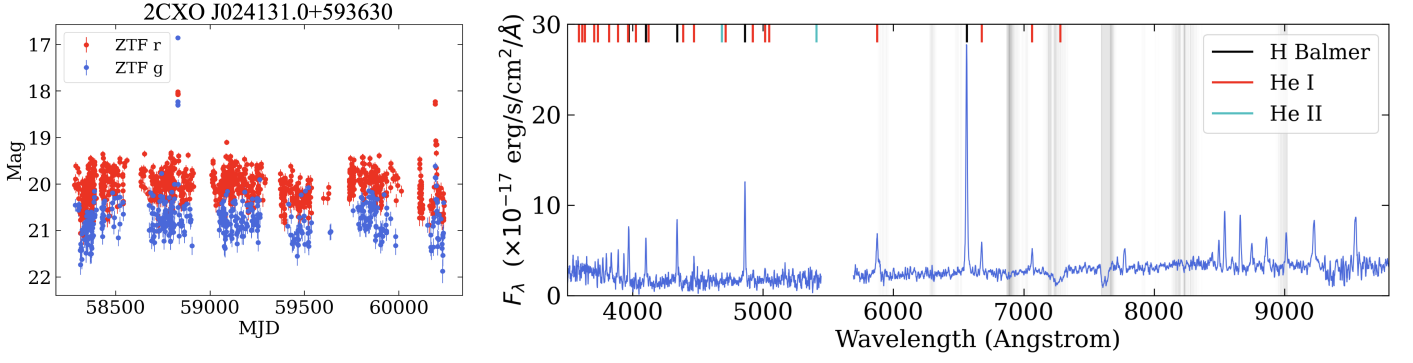


**Fig. B.1.** ZTF long-term light curves in  $g$  and  $r$  filters (left) and DBSP optical spectrum of 2CXO J024131.0+593630 (right). *Grey lines* represent the Keck Telluric Line List. The optical spectrum shows single peaked Hydrogen Balmer emission lines and a weak He II 4686Å emission line, giving a low line ratio HeII /H $\beta$   $\approx$  0.12 (see Table B.2). Our analysis, based on optical and X-ray properties, suggests that J0241 is a new CV, likely non-magnetic (see Section B.1 for more details).

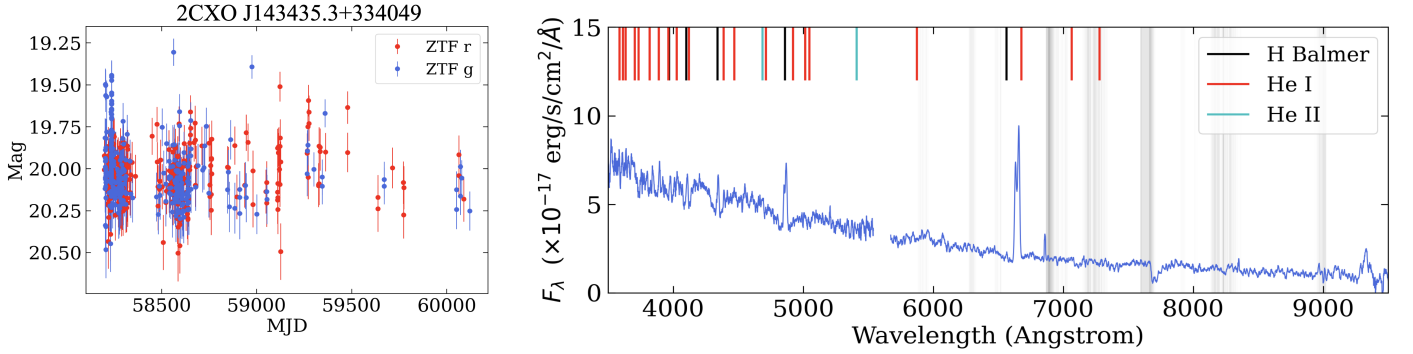


**Fig. B.2.** ZTF long-term (left) in  $g$  and  $r$  filters and the DBSP optical spectrum of 2CXO J143435.3+334049 (right). *Grey lines* represent the Keck Telluric Line List. The optical spectrum shows WD Balmer absorption lines with no sign of the donor signature in the optical spectrum and double-peaked, asymmetric H $\alpha$  and H $\beta$  emission lines. There is no detection of the high-excitation He II 4686Å emission line providing an upper limit for a line ratio HeII /H $\beta$   $<$  0.15 (see Table B.2). X-ray and optical properties suggest that the object is a low-accretion rate CV (WZ Sge type) (see Section B.2 for more details).

**Table B.2.** Equivalent widths of selected lines of two previously known CVs.

Object ID (2CXO)	J024131.0+593630	J143435.3+334049
<i>Line (Å)</i>		
<i>Emission features</i>		
H $\alpha$ 6562.8	$336 \pm 3$	$222 \pm 6$
H $\beta$ 4861.3	$114 \pm 2$	$55 \pm 4$
H $\gamma$ 4340.5	$86 \pm 2$	$< 12$
He I 5876.5	$91 \pm 2$	$< 10$
He I 7065.2	$26 \pm 3$	$9 \pm 2$
He II 4685.7	$14 \pm 4^*$	$< 8$
He II / H $\beta$	$0.12 \pm 0.04^*$	$< 0.15$

**Notes.** (\*) – The measurement is statistically significant, but visual inspection suggests the line is not present.  $3\sigma$  upper limits are shown if no higher significant measurement is detected.

#### Appendix B.2: 2CXO J143435.3+334049, low-accretion rate CV

In Figure B.2 (left panel), we present the long-term ZTF light curve of 2CXO J143435.3+334049 (hereafter J14343). A preliminary Lomb-Scargle period analysis reveals no periodicity in the ZTF data, indicating that further observations are needed to determine the possible orbital period of this system.

We observed J14343 with P200/DBSP on 21 January 2023 for 900s. The optical spectrum of J14343 is presented in Figure B.2 (right panel). The WD Balmer absorption lines are seen with double-peaked emission lines at the center, though the peaks appear to be asymmetric in height and width for both the H $\alpha$  and H $\beta$  lines. We do not detect the high-excitation He II 4686Å emission line providing an upper limit for a line ratio HeII /H $\beta$   $<$  0.15 (see Table B.2). There is no sign of the donor signature in the optical spectrum. The spectrum of this object in Figure B.2 is different from the one shown in Inight et al. (2023), with the Balmer emission lines here being noticeably asymmetric. This could warrant future study of this system to further understand the nature of this source.

J14343 shows a flux ratio  $F_X/F_{\text{opt}} \approx 0.3$  and a lower X-ray luminosity ( $L_X \approx 4.8 \times 10^{29} \text{ erg s}^{-1}$ ) than typically seen in CVs (see Table B.1). We have not detected statistically significant flux and spectral parameter variability between *Chandra* observations. The X-ray spectrum can be approximated by a power-law model with a photon index  $\Gamma \approx 1.7$  (or  $kT \gtrsim 5.2 \text{ keV}$  for optically thin thermal emission model) (see Table C.1 and Figure C.1). X-ray and optical properties suggest that J14343 is a low-accretion rate CV (WZ Sge type), similar to what Inight et al. (2023) concluded in their analysis.

### Appendix B.3: 2CXO J174133.7–284034, a non-magnetic CV

2CXO J174133.7–284034 (hereafter J17413 shows a flux ratio  $F_X/F_{\text{opt}} \approx 1.0$  and an X-ray luminosity  $L_X \approx 4.4 \times 10^{31} \text{ erg s}^{-1}$  (see Table B.1). The X-ray spectrum of J17413 can be approximated by a power-law model with  $\Gamma \approx 1.8$  (or  $kT \approx 5.6 \text{ keV}$  for an optically thin thermal emission model) (see Table C.1 and Figure C.1). We have not detected statistically significant flux and spectral parameter variability between *Chandra* observations. We found no significant period for J17413 with the X-ray timing analysis for the longest exposure *Chandra* observation (ObsID = 9565). Britt et al. (2014) observed optical variability ( $\approx 1 \text{ mag}$ ) with no periodicity. Wevers et al. (2017) observed prominent emission lines and confirmed via optical spectroscopy that J17413 is a CV. Our X-ray analysis supports Britt et al. (2014) and Wevers et al. (2017) conclusions and also suggests that J17413 is likely a non-magnetic system.

### Appendix C: X-ray spectra figures

Figure C.1 shows *Chandra* X-ray spectra of all objects from Tables 1 and B.1. Table C.1 shows the results of the approximation of X-ray spectra with two spectral models: power-law (powerlaw in XSPEC with photon index parameter,  $\Gamma$ ) and optically thin thermal plasma emission model (mekal in XSPEC with temperature  $kT$ , and metal abundance  $[Z]$  parameters).

### References

- Abril, J., Schmidtobreick, L., Ederoclite, A., & López-Sanjuan, C. 2020, MNRAS, 492, L40
- Arnaud, K. A. 1996, in *Astronomical Society of the Pacific Conference Series*, Vol. 101, *Astronomical Data Analysis Software and Systems V*, ed. G. H. Jacoby & J. Barnes, 17
- Astropy Collaboration, Price-Whelan, A. M., Sipőcz, B. M., et al. 2018, AJ, 156, 123
- Astropy Collaboration, Robitaille, T. P., Tollerud, E. J., et al. 2013, A&A, 558, A33
- Bellm, E. C., Kulkarni, S. R., Graham, M. J., et al. 2019, PASP, 131, 018002
- Boldin, P. A., Tsygankov, S. S., & Lutovinov, A. A. 2013, *Astronomy Letters*, 39, 375
- Boller, T., Freyberg, M. J., Trümper, J., et al. 2016, A&A, 588, A103
- Britt, C. T., Hynes, R. I., Johnson, C. B., et al. 2014, ApJS, 214, 10
- Campbell, R. K., Harrison, T. E., Schwöpe, A. D., & Howell, S. B. 2008, ApJ, 672, 531
- Cardelli, J. A., Clayton, G. C., & Mathis, J. S. 1989, ApJ, 345, 245
- Cash, W. 1979, ApJ, 228, 939
- Chambers, K. C., Magnier, E. A., Metcalfe, N., et al. 2016, arXiv e-prints, arXiv:1612.05560
- Chen, B. Q., Huang, Y., Yuan, H. B., et al. 2019, MNRAS, 483, 4277
- Cordova, F. A., Jensen, K. A., & Nugent, J. J. 1981, MNRAS, 196, 1
- Cordova, F. A. & Mason, K. O. 1984, MNRAS, 206, 879
- Dekany, R., Smith, R. M., Riddle, R., et al. 2020, PASP, 132, 038001
- DESI Collaboration, Adame, A. G., Aguilar, J., et al. 2023, arXiv e-prints, arXiv:2306.06308
- DESI Collaboration, Aghamousa, A., Aguilar, J., et al. 2016, arXiv e-prints, arXiv:1611.00036
- Downes, R. A., Webbink, R. F., Shara, M. M., et al. 2001, PASP, 113, 764
- El-Badry, K., Conroy, C., Fuller, J., et al. 2022, MNRAS, 517, 4916
- Evans, I. N., Primini, F. A., Glotfelty, K. J., et al. 2010, ApJS, 189, 37
- Faulkner, J. 1971, ApJ, 170, L99
- Fruscione, A., McDowell, J. C., Allen, G. E., et al. 2006, in *Society of Photo-Optical Instrumentation Engineers (SPIE) Conference Series*, Vol. 6270, *Observatory Operations: Strategies, Processes, and Systems*, ed. D. R. Silva & R. E. Doxsey, 62701V
- Gaia Collaboration, Vallenari, A., Brown, A. G. A., et al. 2023, A&A, 674, A1
- Galiullin, I., Rodríguez, A. C., Kulkarni, S. R., et al. 2024, MNRAS, 528, 676
- Galiullin, I. I. & Gilfanov, M. R. 2021, *Astronomy Letters*, 47, 587
- Gänsicke, B. T., Dillon, M., Southworth, J., et al. 2009, MNRAS, 397, 2170
- Ginsburg, A., Sipőcz, B. M., Brasseur, C. E., et al. 2019, AJ, 157, 98
- Graham, M. J., Kulkarni, S. R., Bellm, E. C., et al. 2019, PASP, 131, 078001
- Green, G. M., Schlafly, E., Zucker, C., Speagle, J. S., & Finkbeiner, D. 2019, ApJ, 887, 93
- Güver, T. & Özel, F. 2009, MNRAS, 400, 2050
- Haberl, F. & Motch, C. 1995, A&A, 297, L37
- Hameury, J. M. 2020, *Advances in Space Research*, 66, 1004
- Harris, C. R., Millman, K. J., van der Walt, S. J., et al. 2020, *Nature*, 585, 357
- HI4PI Collaboration, Ben Bekhti, N., Flöer, L., et al. 2016, A&A, 594, A116
- Hunter, J. D. 2007, *Computing in Science & Engineering*, 9, 90
- Inight, K., Gänsicke, B. T., Schwöpe, A., et al. 2023, MNRAS, 525, 3597
- Israel, G. L., Esposito, P., Rodríguez Castillo, G. A., & Sidoli, L. 2016, MNRAS, 462, 4371
- Ivanova, N., Justham, S., Chen, X., et al. 2013, A&A Rev., 21, 59
- Jackim, R., Szkody, P., Hazelton, B., & Benson, N. C. 2020, *Research Notes of the American Astronomical Society*, 4, 219
- Khamitov, I. M., Bikmaev, I. F., Gilfanov, M. R., et al. 2023, *Astronomy Letters*, 49, 271
- Knigge, C. 2006, MNRAS, 373, 484
- Knigge, C., Baraffe, I., & Patterson, J. 2011, ApJS, 194, 28
- Kupfer, T., Korol, V., Littenberg, T. B., et al. 2023, arXiv e-prints, arXiv:2302.12719
- Larsson, S. 1996, A&AS, 117, 197
- Lazarz, D., Yan, R., Wilhelm, R., et al. 2022, A&A, 668, A21
- Mackereth, J. T., Bovy, J., Leung, H. W., et al. 2019, MNRAS, 489, 176
- Makarov, V. V. & Secrest, N. J. 2022, ApJ, 933, 28
- Maoc, D., Mannucci, F., & Nelemans, G. 2014, ARA&A, 52, 107
- Masci, F. J., Laher, R. R., Rusholme, B., et al. 2019, PASP, 131, 018003
- Merloni, A., Lamer, G., Liu, T., et al. 2024, A&A, 682, A34
- Nasa High Energy Astrophysics Science Archive Research Center (Heasarc). 2014, HEASoft: Unified Release of FTOOLS and XANADU, *Astrophysics Source Code Library*, record ascl:1408.004
- Oke, J. B., Cohen, J. G., Carr, M., et al. 1995, PASP, 107, 375
- Oke, J. B. & Gunn, J. E. 1982, PASP, 94, 586
- Paczynski, B. 1967, *Acta Astron.*, 17, 287
- Paczynski, B. 1976, in *Structure and Evolution of Close Binary Systems*, ed. P. Eggleton, S. Mitton, & J. Whelan, Vol. 73, 75
- Parsons, S. G., Gänsicke, B. T., Schreiber, M. R., et al. 2021, MNRAS, 502, 4305
- Patterson, J. 1998, PASP, 110, 1132
- Perley, D. A. 2019, PASP, 131, 084503
- Predehl, P., Andritschke, R., Arefiev, V., et al. 2021, A&A, 647, A1
- Pretorius, M. L. & Knigge, C. 2012, MNRAS, 419, 1442
- Prochaska, J., Hennawi, J., Westfall, K., et al. 2020, *The Journal of Open Source Software*, 5, 2308
- Queiroz, A. B. A., Anders, F., Chiappini, C., et al. 2020, A&A, 638, A76
- Ramsay, G., Green, M. J., Marsh, T. R., et al. 2018, A&A, 620, A141
- Rappaport, S., Verbunt, F., & Joss, P. C. 1983, ApJ, 275, 713
- Ritter, H. & Kolb, U. 2003, A&A, 404, 301
- Rodríguez, A. C. 2024, PASP, 136, 054201
- Rodríguez, A. C., Galiullin, I., Gilfanov, M., et al. 2023a, ApJ, 954, 63
- Rodríguez, A. C., Kulkarni, S. R., Prince, T. A., et al. 2023b, ApJ, 945, 141
- Schreiber, M. R., Belloni, D., Gänsicke, B. T., Parsons, S. G., & Zorotovic, M. 2021, *Nature Astronomy*, 5, 648
- Schreiber, M. R., Belloni, D., & Schwöpe, A. D. 2024, A&A, 682, L7
- Schreiber, M. R., Zorotovic, M., & Wijnen, T. P. G. 2016, MNRAS, 455, L16
- Schwöpe, A., Buckley, D. A. H., Kawka, A., et al. 2022a, A&A, 661, A42
- Schwöpe, A., Buckley, D. A. H., Malyali, A., et al. 2022b, A&A, 661, A43
- Smethurst, R. J., Masters, K. L., Simmons, B. D., et al. 2022, MNRAS, 510, 4126
- Souchay, J., Secrest, N., Lambert, S., et al. 2022, A&A, 660, A16
- Sprague, D., Culhane, C., Kounkel, M., et al. 2022, AJ, 163, 152
- Spruit, H. C. & Ritter, H. 1983, A&A, 124, 267
- Stone-Martinez, A., Holtzman, J. A., Imig, J., et al. 2024, AJ, 167, 73
- Sunyaev, R., Arefiev, V., Babyshkin, V., et al. 2021, A&A, 656, A132
- Walter, F. M. & Bowyer, S. 1981, ApJ, 245, 671
- Warner, B. 2003, *Cataclysmic Variable Stars*
- Weisskopf, M. C., Brinkman, B., Canizares, C., et al. 2002, PASP, 114, 1
- Weisskopf, M. C., Tananbaum, H. D., Van Speybroeck, L. P., & O'Dell, S. L. 2000, in *Society of Photo-Optical Instrumentation Engineers (SPIE) Conference Series*, Vol. 4012, *X-Ray Optics, Instruments, and Missions III*, ed. J. E. Truemper & B. Aschenbach, 2–16
- Wenger, M., Ochsenbein, F., Egret, D., et al. 2000, A&AS, 143, 9
- Wevers, T., Torres, M. A. P., Jonker, P. G., et al. 2017, MNRAS, 470, 4512
- Wilms, J., Allen, A., & McCray, R. 2000, ApJ, 542, 914
- Yang, H., Hare, J., Kargaltsev, O., et al. 2022, ApJ, 941, 104

**Table C.1.** Results of approximation of X-ray spectra of objects from Tables 1 and B.1 by different models.

Name (2CXO)	J024131.0+593630	J044048.3+292434	J044147.9–015145	J063805.1–801854	J094607.7–311550	J104435.5–594045
<b>ObsID</b>	7152 + 7369	12677	11676	14925	15383	4495 + 6402
<b>tbabs x powerlaw</b>						
$N_H(\times 10^{22} \text{ cm}^{-2})$	$0.42 \pm 0.11$	$0.18^b$ (fixed)	$0.04^b$ (fixed)	$\leq 0.01$	$0.03$ (fixed)	$0.05$ (fixed)
$\Gamma$	$1.78 \pm 0.14$	$0.54 \pm 0.19$	$1.78^{+0.23}_{-0.22}$	$0.22^{+0.05}_{-0.08}$	$0.48^{+0.40}_{-0.41}$	$1.77^{+0.38}_{-0.37}$
C-stat/dof	153.25/153	29.27/24	22.09/21	196.92/132	1.45/10	45.08/35
<b>tbabs x mekal</b>						
$N_H(\times 10^{22} \text{ cm}^{-2})$	$0.35^{+0.09}_{-0.08}$	$0.18^b$ (fixed)	$0.04^b$ (fixed)	$0.45^{+0.08}_{-0.07}$	$0.03$ (fixed)	$0.05$ (fixed)
kT(keV)	$5.54^{+1.12}_{-0.83}$	$\geq 55.54$	$4.54^{+3.47}_{-1.46}$	$\geq 74.80$	$\geq 24.92$	$3.50^{+4.09}_{-1.29}$
$Z(Z_\odot)$	$2.90^{+1.91}_{-1.21}$	$1.0$ (fixed)	$1.0$ (fixed)	$1.0$ (fixed)	$1.0$ (fixed)	$1.0$ (fixed)
C-stat/dof	144.18/152	42.83/24	21.55/21	314.20/132	4.93/10	43.49/35
Name (2CXO)	J123727.5+655211	J143435.3+334049	J155926.5–754311	J165219.0–441401	J173118.6+224248	J173332.5–181735
<b>ObsID</b>	6817 + 20443 <sup>c</sup>	4236 + 19645 <sup>c</sup>	14386	8145	3281	12944
<b>tbabs x powerlaw</b>						
$N_H(\times 10^{22} \text{ cm}^{-2})$	$0.08^{+0.06}_{-0.05}$	$0.009^a$ (fixed)	$0.06^a$ (fixed)	$0.79^{+0.32}_{-0.29}$	$0.17^{+0.15}_{-0.13}$	$0.27^{+0.07}_{-0.06}$
$\Gamma$	$1.36 \pm 0.06$	$1.71^{+0.32}_{-0.31}$	$1.95^{+0.77}_{-0.67}$	$1.53^{+0.35}_{-0.33}$	$2.23^{+0.34}_{-0.31}$	$1.36 \pm 0.12$
C-stat/dof	394.68/367	16.67/16	5.70/4	26.22/29	34.85/35	146.50/138
<b>tbabs x mekal</b>						
$N_H(\times 10^{22} \text{ cm}^{-2})$	$\leq 0.08$	$0.009^a$ (fixed)	$0.06^a$ (fixed)	$0.89^{+0.32}_{-0.27}$	$\leq 0.12$	$0.26^{+0.05}_{-0.06}$
kT(keV)	$38.28^{+31.40}_{-13.15}$	$\geq 5.16$	$\geq 2.00$	$5.78^{+6.48}_{-2.01}$	$2.97^{+0.88}_{-0.75}$	$20.82^{+51.70}_{-8.61}$
$Z(Z_\odot)$	$\leq 1.46$	$1.0$ (fixed)	$1.0$ (fixed)	$4.16^{+10.75}_{-3.12}$	$1.24^{+1.92}_{-0.90}$	$\leq 15.59$
C-stat/dof	397.16/366	18.52/16	5.89/4	23.93/28	30.63/34	146.34/137
Name (2CXO)	J173555.3–292530	J174133.7–284034	J182117.2–131405	J185603.2+021259	J190823.2+343328	
<b>ObsID</b>	8703 + 8704	9564 + 9565 + 21605 <sup>c</sup>	7561	9613	13659	
<b>tbabs x powerlaw</b>						
$N_H(\times 10^{22} \text{ cm}^{-2})$	$0.002$ (fixed)	$0.21 \pm 0.06$	$0.03$ (fixed)	$0.005$ (fixed)	$0.01$ (fixed)	
$\Gamma$	$0.58 \pm 0.51$	$1.78^{+0.10}_{-0.09}$	$1.74^{+0.88}_{-0.79}$	$2.79^{+0.64}_{-0.63}$	$1.15^{+0.25}_{-0.24}$	
C-stat/dof	4.02/6	275.22/273	1.34/1	1.98/2	19.04/17	
<b>tbabs x mekal</b>						
$N_H(\times 10^{22} \text{ cm}^{-2})$	$0.002$ (fixed)	$0.13 \pm 0.04$	$0.03$ (fixed)	$0.005$ (fixed)	$0.01$ (fixed)	
kT(keV)	$\geq 14.69$	$5.62^{+0.77}_{-0.62}$	$\geq 1.60$	$1.04^{+1.22}_{-0.27}$	$\geq 18.01$	
$Z(Z_\odot)$	$1.0$ (fixed)	$2.61^{+1.21}_{-0.83}$	$1.0$ (fixed)	$1.0$ (fixed)	$1.0$ (fixed)	
C-stat/dof	5.65/6	247.52/270	1.24/1	4.12/2	19.28/17	

**Notes.** (a) –  $N_H$  is fixed at Galactic hydrogen column density; (b) – Color excess  $E(B - V)$  from the Bayestar dust map lies outside the reliable distance interval, so we fixed  $N_H$  at Galactic hydrogen column density; (c) – New *Chandra* observation is used in the analysis, which is not presented in CSC2.

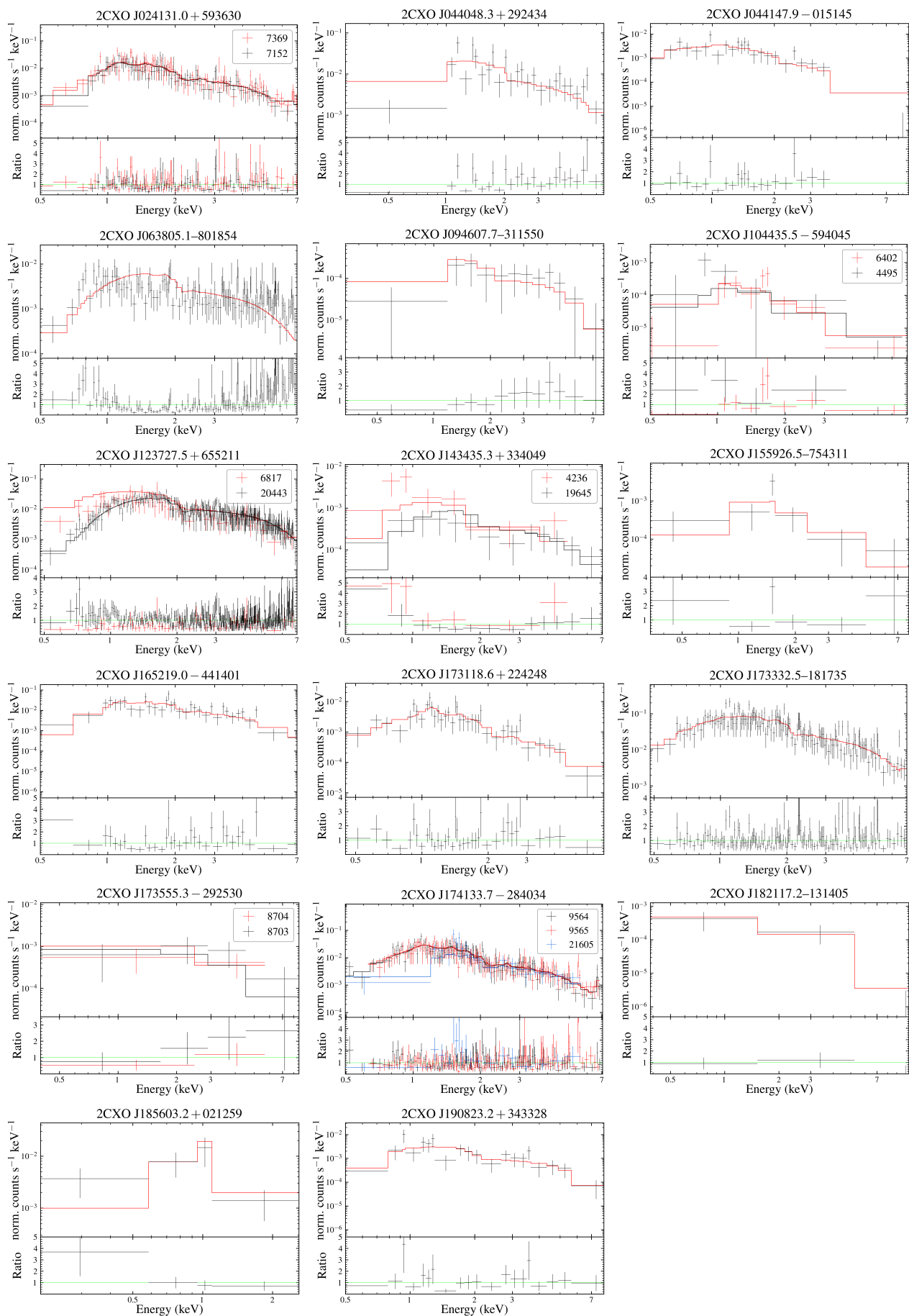


**Fig. C.1.** The *Chandra* X-ray spectra of objects from Tables 1 and B.1 (top panel). The solid lines show the best-fit mekal model. The bottom panel shows the ratio of the data divided by the model in each energy channel.